Title: Ionizable networks mediate pH-dependent allostery in SH2 signaling proteins

One-sentence summary: This paper investigates the role of pH in the allosteric regulation of signaling proteins with SH2 domains, specifically focusing on SHP2 and Src

Papa Kobina Van Dyck[1,2], Luke Piszkin[1], Elijah A. Gorski[1,2], Eduarda Tartarella Nascimento[1,2,3], Joshua A. Abebe[1,2], Logan M. Hoffmann[1,2], Jeffrey W. Peng[1], Katharine A. White[1,2,*]

1 Department of Chemistry and Biochemistry, University of Notre Dame
251 Nieuwland Science Hall Notre Dame, IN 46556 USA

2 Harper Cancer Research Institute, University of Notre Dame
1234 N. Notre Dame Avenue South Bend, IN 46617 USA

3 Saint Mary's College, Notre Dame, IN 46556 USA

*Corresponding Author: kwhite6@nd.edu

Abstract

Intracellular pH dynamics regulate normal cell biology, but most molecular drivers remain unknown. We developed a computational pipeline to identify pH-sensitive proteins and their mechanisms. We applied the pipeline to SHP2, a pH-sensitive signaling protein, with unknown mechanism. We found that SHP2 phosphatase activity is pH-sensitive in vitro and in cells, and mutation of identified His116 and Glu252 abolishes pH-sensitive function. We also discovered that Src is an unrecognized pH-dependent kinase and mutation of the identified ionizable network abolishes pH-sensitive activity. Importantly, we found that Src kinase activity was pH sensitive even in the presence of EGF and with a phosphomimetic (Src-Y527E) mutant required for auto-inhibitory SH2 domain binding. Thus, the identified pH-sensitive regulation of Src kinase activity functions in concert with established mechanisms of Src regulation by phosphorylation. Constant pH molecular dynamics simulations performed on both SHP2 and Src support allosteric regulation mediated by pH-dependent binding of inhibitory SH2 domains to the respective catalytic domains. Finally, we show that evolutionarily conserved putative pH-sensing networks were identified across SH2 domain-containing signaling proteins. Taken together, our computational, biophysical, and cellular analyses reveal a role for pHi dynamics in allosterically regulating activity of modular SH2 signaling proteins to control biology.

57 **Introduction**

58 Transient intracellular pH (pHi) dynamics(*1*) regulate mammalian proliferation(*2*, *3*),
59 migration(*4*), and differentiation(*5*). However, for many pH-dependent cell processes, the
60 molecular mediators are unknown(*6*). All proteins have ionizable residues that can bind or
61 release protons, thereby changing their charged state. For an ionizable residue to have pH-
62 dependent biological function, the H^+ binding affinity (pK_a) of one or more residues must be in
63 the physiological pH range (6.8-8.0). It is not surprising that most cytoplasmic pH-sensitive
64 proteins (pH sensors) with characterized molecular mechanisms function through titratable
65 histidine residues (solution pK_a of 6.5). However, the pK_as of ionizable residues are sensitive to
66 electrostatic microenvironment(*7*). Thus, local protein microenvironment can up- or down-shift
67 pK_as of glutamates, aspartates, and lysines into the physiological pH range(*8–12*). Further
68 complicating this pH sensing landscape, ionizable residues can cooperatively regulate pH-
69 dependent membrane proteins(*13*, *14*) and can be sequestered within cytoplasmic protein cores
70 or buried at the interface of protein-protein complexes(*15*). However, complex networks of
71 ionizable residues are difficult to identify *a priori* based on structure-gazing, and thus many
72 cytoplasmic proteins known to have pH-sensitive function have unknown or incompletely
73 characterized molecular mechanisms.

74

75 **Results**

76 **Pipeline to identify putative pH-sensitive networks**

77 To more quickly identify pH-sensitive proteins and characterize unknown pH sensing
78 mechanisms, we developed an in silico prediction pipeline to identify putative pH sensing nodes
79 based on 3D protein structure (**Fig. 1A**, see methods for details).

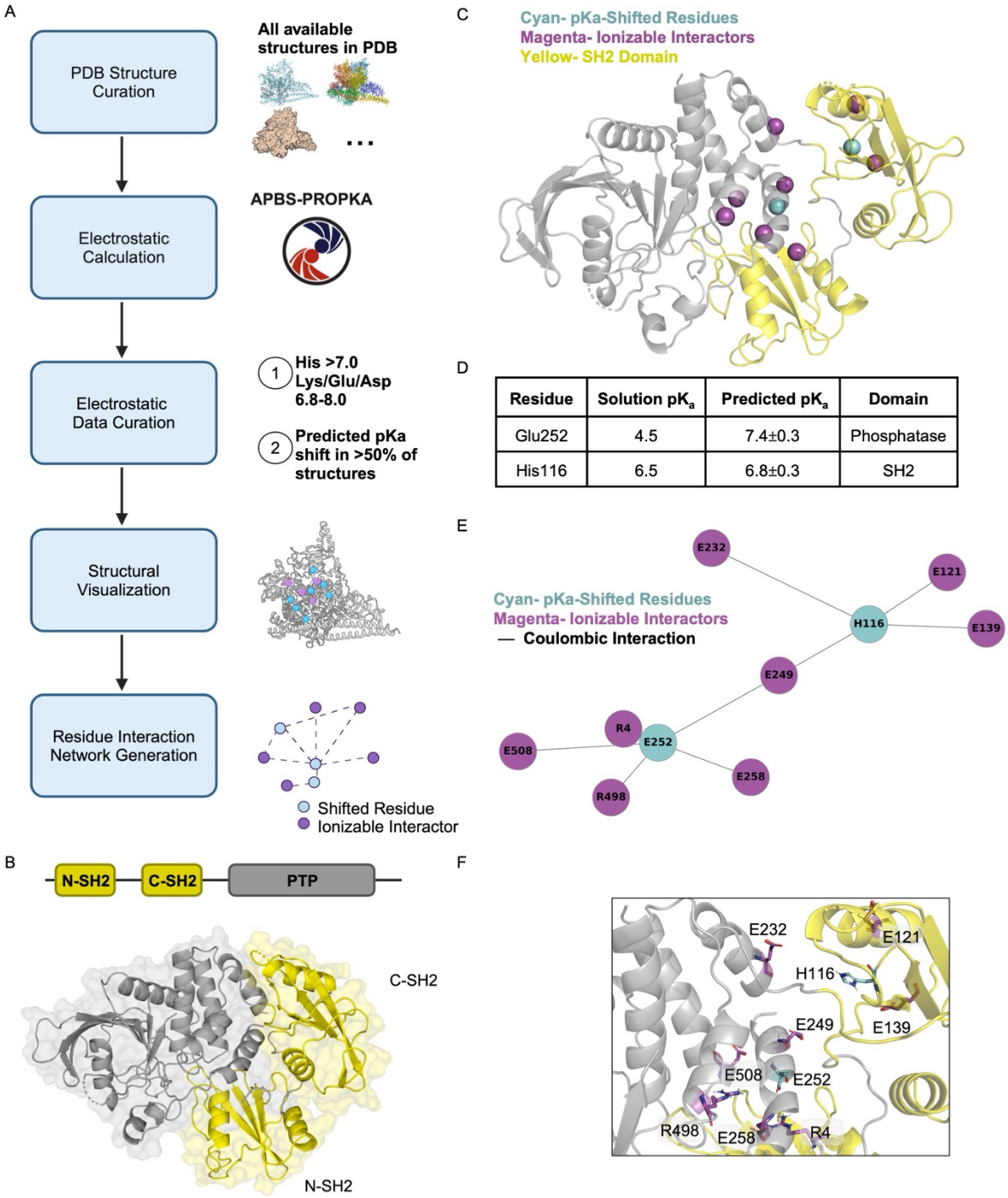

Residue	Solution pK_a	Predicted pK_a	Domain
Glu252	4.5	7.4±0.3	Phosphatase
His116	6.5	6.8±0.3	SH2

Figure 1. New pipeline to identify pH-sensitive networks predicts SHP2 His116 and Glu252 have physiological pK_as. (A) Schematic for in silico pK_a prediction method for proteins with solved structures. Briefly, all available structures in the protein database are curated, electrostatic properties are calculated using PROPKA, results are filtered for ionizable residues with physiologically relevant predicted pK_a values, and data are visualized in a 3D structure or a 2D

residue interaction network. (B) Crystal structure of SHP2 shown in cartoon and surface format (PDB ID:2SHP). Protein tyrosine phosphatase (PTP) domain colored in grey, SH2 domains colored in yellow. (C) Structure of SHP2 (PDB ID:2SHP) with protein tyrosine phosphatase (PTP) domain in grey and SH2 domains in yellow. Residues identified through in silico ionizable network prediction pipeline shown in spheres. Residues with predicted pK_a shifts (cyan) cluster with ionizable interactors (magenta) across the phosphatase-SH2 domain interaction interface of SHP2. (D) Table of predicted pK_as for cyan residues identified using *in silico* ionizable network prediction pipeline on 47 SHP2 structures (mean ± SD). (E) Residue interaction network of residues with predicted pK_a shifts (cyan) and their ionizable interactors (magenta). Length of edges reflect the strength of the coulombic interaction, with stronger coulombic interactions having shorter edge lengths (F) Zoom of SHP2 structure at the PTP-SH2 interaction interface. Networked residues from C and E are shown in stick. Residues with predicted pK_a shifts in cyan and ionizable interactors in magenta.

Briefly, we use PROPKA(*16*) to predict the pK_as of ionizable groups based on available structure(s) of a protein of interest. Next, we filter these results for buried ionizable residues with physiological pK_as and generate 2D and 3D maps showing the identified residue networks and other ionizable coulombic interactors. We can perform this pipeline on multiple full-length structures of the protein of interest, increasing the likelihood of identifying functional networks. Through the generation of interaction network maps and structural maps, our pipeline provides meaningful perspectives on the functional roles of pH-sensing residues based on their location and clustering within the protein.

Our pipeline leverages structural flexibility through the analysis of multiple solved protein structures and integrates PROPKA3 for efficient pKa estimation. Previous studies collected experimental pK_a values from a diverse set 34 proteins with 290 experimentally determined pK_as for Asp, Glu, His, Tyr and Lys residues (*17*). Using our pipeline, we calculated the pK_as for these previously determined ionizable residues and found that our pipeline achieves high accuracy, with a correlation coefficient of 0.954 and a root-mean-square deviation (RMSD) of 0.888 (**Fig. S1A, B**). The majority of proteins in this dataset had pK_a shifts of less than 1.5 pH

116 units, with just a few residues exhibiting shifts of up to 3.5 pH units (*17*). The Garcia-Moreno lab
117 previously used NMR to measure pK_as of buried ionizable residues in Staphylococcal nuclease
118 (SNase) mutants, and found large shifts in pKas (up to 5 pH units) from their solution pK_a values
119 (*18–20*). To determine whether our pipeline can accurately predict large pK_a shifts, we compared
120 the delta pK_as of the SNase NMR dataset against our predictive pipeline and found that our
121 pipeline generally had strong correlation values with an overall RMSD of 1.6 pH units (**Fig.**
122 **S1C, D**). Furthermore, we found that the pipeline accurately identified whether the residue was
123 far upshifted or far downshifted. Importantly, there was no bias in pKa calculation errors using
124 our pipeline for histidines, aspartates, and glutamates compared to experimental pKas in the
125 SNase dataset. Our pipeline consistently under-predicted lysine pKa shifts compared to
126 experimental pKas determined for the SNase dataset (**Fig. S1C**), though no such bias was found
127 for lysine residues in the more diverse protein dataset (**Fig. S2A**).

128 The performance of our pipeline compares favorably to prior work developing a
129 computationally complex pKa prediction programs (Rosetta pH, RMSD 0.85) (*17*). While multi-
130 conformation continuum electrostatic (MCCE) calculations have been frequently used to analyze
131 pKa shifts based on protein structures (*21*, *22*), MCCE is computationally expensive and does
132 not achieve improved RMSDs compared to our computationally inexpensive approach. RMSDs
133 from "quick calculation" MCCE are generally >1.3 pH units, and calculations including rotamers
134 and side chain optimization are required to achieve RMSDs <1.0 pH unit by MCCE (*21*). Similar
135 computationally efficient approaches have been developed to predict protein pKas such as
136 pHinder (*13*) and BRIDGE (*23*), both arising from work on membrane proteins. Unlike these
137 approaches, our approach is agnostic to protein localization and does not require a path for
138 structural waters from bulk solvent to the identified buried ionizable networks(*13*, *24*).

139 Thus, our computational pipeline offers a comprehensive and efficient approach to
140 identify residues with predicted physiological pKas that may function as pH-sensitive residues in
141 proteins. Through the generation of interaction network maps and structural maps (**Fig. 1A**), our
142 pipeline provides meaningful information to identify putative pH-sensing residues and link them
143 to protein function based on their location and clustering within the protein. We next applied our
144 pipeline to predict pH-sensing mechanisms and identify novel pH sensitive proteins.
145

146 **Analysis pipeline applied to SHP2 identifies His116 and Glu252 with predicted upshifted**
147 **pK_as**

148 We first applied our analysis pipeline to the SH2 domain-containing signaling protein SHP2.
149 SHP2 is a regulator of multiple pH-sensitive processes including cell proliferation, migration,
150 differentiation, growth, and survival(*25–27*). SHP2 has also been shown to have pH-dependent
151 phosphatase activity in vitro, with optimal activity at pH 7.0 and decreasing activity both below
152 and above 7.0(*28*), suggestive of multi-group titration. While SHP2 activity is pH sensitive in
153 vitro, the pH-dependent molecular mechanism has not been identified. Furthermore, prior work
154 showed that SHP2 activity positively regulates endothelial cell migration and angiogenesis and
155 vascular smooth muscle cell function(*26*), but the role for pH-sensitive SHP2 function in cells is
156 less clear.

157 SHP2 consists of three globular domains: a protein tyrosine phosphatase (PTP) domain
158 responsible for catalyzing the dephosphorylation of tyrosine-phosphorylated proteins, and two
159 Src Homology 2 (SH2) domains that serve as phosphotyrosine (pTyr)-recognition domains(*29*)
160 (**Fig. 1B**). In the absence of a tyrosine-phosphorylated binding partner, the N-terminal SH2
161 domain binds directly to the phosphatase domain, blocking the active site(*30*). Upon ligand-

162 induced receptor activation or signaling events, the SH2-PTP interaction is disrupted when the
163 SH2 domains are displaced by a tyrosine phosphorylated binding partner(*30*). Thus, the SH2
164 domains control SHP2 activity by allosterically inhibiting the PTP domain in the bound state and
165 influencing SHP2 localization via direct interactions with phosphorylated binding partners when
166 signaling active(*30*).

167 Because SHP2 has no known molecular mechanism of pH-sensing, our goal was to identify
168 the putative pH sensing nodes driving SHP2 pH-dependent phosphatase activity. We processed
169 47 structures of SHP2 available in the PDB through the computational pipeline. Importantly, we
170 did not filter the structural input data: SHP2 structures included active conformations, inhibited
171 conformations, and SHP2 proteins with gain- or loss-of-function mutations. Our analysis
172 revealed a conserved network of ionizable residues clustering at the interface between the SH2
173 and PTP domains of SHP2 (**Fig. 1C**). This residue network contained two residues with
174 predicted physiological pK_as: His116 and Glu252, with predicted pK_as of 6.8±0.3 and 7.4±0.3,
175 respectively (**Fig. 1D**). His116 is in the C-SH2 domain and directly interacts with a cluster of
176 glutamate residues (E121, E139, E232, and E249). Similar glutamate "cages" have been
177 identified in other wild-type pH sensors including talin(*31*) and RasGRP1(*32*). Glu252 is in the
178 phosphatase domain at the interaction interface with the N-SH2 domain and interacts with R4,
179 E249, E258, R498, and E508 (**Fig. 1E, F**). We next determined the structural conservation of the
180 identified residues using Consurf(*33*). Analyses of structural conservation can frequently reveal
181 functionally important regions, such as catalytic and ligand-binding sites(*33*). We found that the
182 C-SH2 and N-SH2 are both highly conserved at the interaction interface with the PTP domain
183 (**Fig. S2A**). We also determined that His116 and Glu252 are sequence-conserved across SHP2
184 from lower-order organisms (**Fig. S2A-C**). Taken together, these data suggest that the SH2

185 domain binding interface in SHP2 has an evolutionarily conserved network of ionizable residues
186 with predicted physiological pK_as.
187
188 **SHP2 pH sensitive function requires both His116 and Glu252**
189 We hypothesized that the previously uncharacterized pH-dependent molecular
190 mechanism of SHP2 requires the ionizable network identified using our computational pipeline.
191 We first assessed the in vitro phosphatase activity of wild-type SHP2 under different buffer pH
192 (pH 6.1-8.0) using a generic para-nitrophenyl phosphate (PNPP) substrate. We found that wild-
193 type SHP2 phosphatase activity is pH dependent, with maximal activity at pH 6.7 and reduced
194 activity both above and below this value (**Fig. 2A, C, S3A**). We found that k_{cat} increased from
195 pH 6.1 through 6.7 and decreased from 7.0 through 8.0 forming a biphasic activity curve **(Fig.**
196 **2C)**, while K_m for the PNPP was pH-insensitive (**Fig. S3A**). This result confirmed previous in
197 vitro characterization of SHP2 activity(*28*), showing similar apparent pK_as of ~6.7 and ~7.1 in
198 both the k_{cat} (**Fig. 2A, C, S3B**) and catalytic efficiency (k_{cat}/K_m) pH profiles (**Fig. S3C**).
199 Reactions with bovine serum albumin (BSA) addition showed no pH-dependence, confirming
200 that buffer pH is not independently affecting non-enzymatic PNPP hydrolysis in these assays
201 (**Fig. S3D**). To test whether the identified network is responsible for SHP2 pH-dependent
202 activity, we generated a SHP2 double mutant where both H116 and E252 were mutated to non-
203 titratable alanine residues. We repeated the phosphatase assay and found that the activity of
204 SHP2-H116A/E252A was pH-independent (**Fig. 2B**). While k_{cat} of SHP2-H116A/E252A was
205 reduced compared to WT SHP2, there was no pH-dependence of k_{cat}, K_m, or catalytic efficiency
206 (**Fig. 2B, C, S3A, S3C)**. This demonstrates that H116 and E252 are required for pH-dependent
207 activity of SHP2.

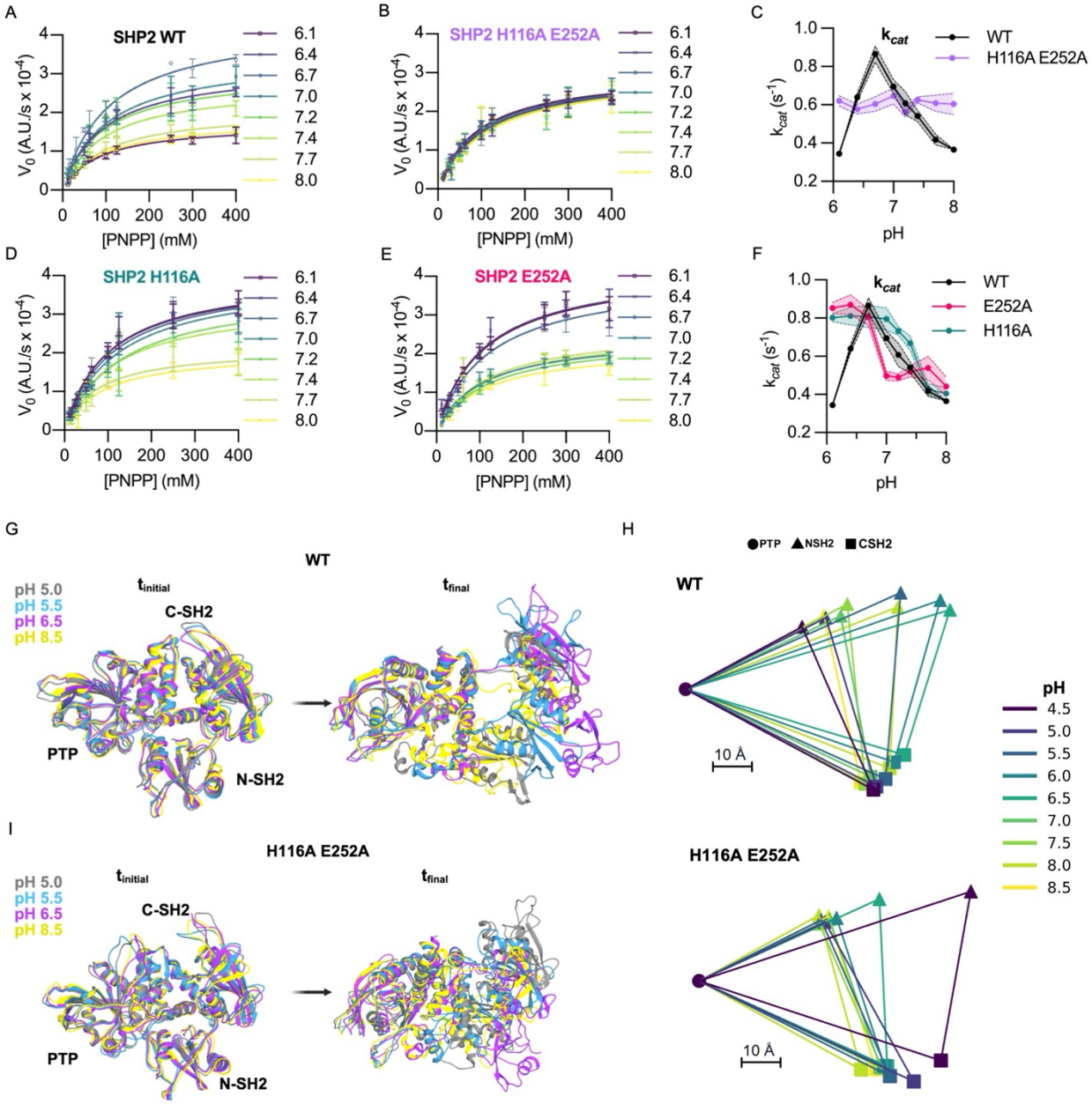

208

209 ***Figure 2. Molecular mechanism of SHP2 pH sensing requires both His116 and Glu252***. (A)
210 Wild-type (WT) SHP2 in vitro phosphatase activity curves with increasing concentrations of
211 generic substrate p-Nitrophenyl Phosphate (PNPP) at buffer pH ranging from 6.1 to 8.0. (mean ±
212 SEM; N=3 from ≥2 different protein preparations) (B) Double mutant (H116A E252A SHP2) in
213 vitro phosphatase activity, assays performed as in A. (mean ± SEM; N=3 from ≥2 different
214 protein preparations) (C) Plot of k_{cat} vs. pH for WT and double mutant (H116A E252A SHP2).
215 Calculated from activity curves in A and B. (mean ± SEM) (D-E) Single-mutant in vitro
216 phosphatase activity for (D) H116A-SHP2 and (E) E252A-SHP2. Assays performed as in A.
217 (mean ± SEM; N=3 from ≥2 different protein preparations) (F) Plot of K_{cat} vs. pH for WT and

218 single mutant H116A SHP2 and E252A SHP2. Calculated from activity curves in A, D and E.
219 (mean ± SEM) (G) CpHMD was performed on WT SHP2 at pH values from 4.0-10.0. Shown are
220 overlapping views of WT SHP2 structures at the start of CpHMD simulation (t = 0 ns) and end
221 of simulation (t = 8 ns) for pH values 5.0 (grey), 5.5 (cyan), 6.5 (magenta) and 8.5 (yellow). (H)
222 Average Interdomain center of mass distances for WT and H116A E252A SHP2 for the last 3 ns
223 of the simulation (I) CpHMD was performed on H116A E252A SHP2 at pH values from 4.0-
224 10.0. Shown are overlapping views of H116A E252A SHP2 structures at the start of CpHMD
225 simulation (t = 0 ns) and end of simulation (t = 8 ns) for pH values 5.0 (grey), 5.5 (cyan), 6.5
226 (magenta) and 8.5 (yellow).
227

228 Our in silico pK_a prediction analysis suggests that H116 and E252 function within
229 networks of conserved ionizable residues. To probe this interaction network in more detail, we
230 next generated the single point mutants (SHP2-H116A and SHP2-E252A) and found that both
231 mutants retained pH-dependent phosphatase activity, but each with a single apparent pK_a (**Fig.**
232 **2D-F**). For both mutants, k_{cat} was maximal at low buffer pH and reduced with increasing pH
233 (**Fig. 2F, S3A, S3C**). We predicted that the pH-dependent activity observed in the single point
234 mutants reflects the pK_a of the remaining titratable residue. We compared apparent pK_as of the
235 mutants and found that SHP2-H116A mutant had an apparent pK_a of 7.5 (**Fig. 2F, S3A, S3E**),
236 which correlates with the higher apparent (pK_{a2}) of wild-type SHP2 (~7.1) and the in silico
237 predicted pK_a of E252 (~7.4) (**Fig. 1D**). The E252A mutant has a lower apparent pK_a of 6.8 (**Fig.**
238 **2F, S3A, S3E**), which matches the lower apparent (pK_{a1}) of the wild-type SHP2 (~6.7), and the
239 in silico predicted pK_a of His116 (6.8) (**Fig. 1D).** This suggests that in the H116A point mutant,
240 E252 drives the observed pH-dependent activity while in the E252A point mutant, H116 drives
241 the observed pH-dependent activity. Compared to the wild-type SHP2 activity profiles, this
242 suggests that H116 titration regulates activity between pH 6.1 to 7.0 while E252 titration
243 regulates activity between pH 7.0 to 8.0. Thus, Glu252 and His116 function cooperatively to
244 confer wild-type SHP2 pH-dependent activity.

245 Because E249 interacts with both Glu252 and His116, we next explored the role this
246 bridging glutamate plays in the pH sensing mechanism of SHP2. Interestingly, we observed
247 similar pH-dependent activity profiles of SHP2-E249A compared to WT (**Fig. S2A, F**). The
248 E249A mutant was still pH sensitive with biphasic k_{cat} and catalytic efficiency pH profiles (**Fig.**
249 **S3C, S3G**). However, the apparent pK_{a1} and pK_{a2} of the E249A mutant were both shifted higher
250 (6.8 and 7.7) when compared to wild-type SHP2 (6.7 and 7.1) (**Fig. S3A, S3C**). This suggests
251 that E249 is not acting as a direct proton conduit or relay between the identified pH sensing
252 residues (H116 and E252) but instead the presence of E249 tunes the pK_a values of these residues
253 through the interaction network.
254
255 **CpHMD reveals pH-dependent residue conformations and SH2 domain release in SHP2**
256 Due to the clustering of pH-sensitive residues at the SH2 and PTP domain interface, we
257 hypothesized that pH-dependent binding of the inhibitory SH2 domains drives pH-dependent
258 SHP2 activity. We used continuous constant pH molecular dynamics (CpHMD) to probe pH-
259 dependent structural conformations of wild-type SHP2. In classical molecular dynamics (MD)
260 simulations, solvent pH is considered implicitly by fixing protonation states based on empirical
261 or predicted residue pK_a values. However, protein conformational dynamics may depend
262 explicitly on residue protonation states, so conventional MD methods cannot capture how
263 dynamic changes in residue protonation affect structural dynamics. CpHMD addresses this gap
264 by sampling protonation and conformation states simultaneously(*34*) and lends insight into
265 proton-coupled mechanisms that are not captured in conventional MD methods.
266 We performed CpHMD simulations of SHP2 using the GBNeck2 implicit solvent model
267 for pH values ranging from 4.0 to 10 (in increments of 0.5) (based on(*34*), see methods;

268 trajectories in **Movies 1-13**). Each simulation was run for 8 nanoseconds, allowing for
269 convergence of backbone RMSD and protonation states, for an aggregate 104 nanoseconds of
270 total simulation time. In agreement with the in vitro results, the pK_a values calculated from SHP2
271 CpHMD showed that H116 had a lower pK_a (6.0) compared to E252 (8.4) (**Fig. S4A, S4B**). In
272 addition, we observed and quantified coordinated pH-dependent changes in the side chain
273 conformations of H116 and E252. (**Fig. S4C-D**). At low (4.5) and high (8.5) pH, H116 and E252
274 are pointed toward each other, but at optimal pH for activity (6.5), E252 flips out and H116
275 swings in, disrupting its local helix (**Fig. S4C-D**). From the CpHMD trajectories, we noted that
276 the SH2 domain remains rigid and tightly bound to the PTP domain at pH values less than 5.5
277 and higher than 8.0 (**Fig. 2G-H**, **Movie4 (2SHP_pH5.5) and Movie9 (2SHP_pH8.0)**).
278 However, at optimal activity pH (6.5) the SH2 domain is more dynamic and loosely bound to the
279 PTP domain (**Fig. 2G-H, Movie6 (2SHP_pH6.5**)). To assess interdomain conformations, we
280 quantified the center of mass distances between the N-SH2 or C-SH2 domain and the PTP
281 domain during the final 3 nanoseconds of the trajectories. We found distinct pH-dependent
282 dynamics between the N-SH2 and PTP domain, with maximal interdomain distances (65Å) at pH
283 6.5 and minimal distances (30Å and 35Å) at pH 4.5 and 8.5 respectively (**Fig. 2H, S4E)**. We
284 observed that dynamics between the C-SH2 and PTP domain followed the same pH-dependent
285 trend, with maximal distances (54Å) achieved at pH 6.5 **(Fig. 2H, S4F).** While interdomain
286 orientations were not included in this analysis, the interdomain distance trends alone suggest pH-
287 dependent SH2 domain release and are in striking agreement with pH-dependent in vitro WT
288 SHP2 activity experiments.
289 We also performed CpHMD simulations for the H116A E252A SHP2 mutant using the
290 same protocol as for WT to determine if these mutations also abrogate the pH dependent

291 interdomain dynamics in silico. Encouragingly, we observed that double mutant exhibited a more
292 closed domain conformation when compared to WT across the pH range 6.0-8.0 (**Fig. 2 H-I,**
293 **S5A-C**). Importantly, the double mutant did not exhibit the strong pH-dependent inter-domain
294 dynamics that we observed with WT SHP2 (**Fig. 2H-I**). Our CpHMD results indicate a loss of
295 pH-dependent interdomain dynamics in the mutant protein, which is in agreement with the in
296 vitro activity results. Taken together, our CpHMD data support a molecular mechanism by which
297 WT SHP2 has pH-dependent SH2 domain binding, with His116 and E252 being required for pH-
298 dependent SH2 domain conformational dynamics.
299

300 **Intracellular pH regulates SHP2 activity and downstream signaling in MCF10A cells**

301 We next determined whether SHP2 activity is regulated by physiological pH changes in
302 cells. We first experimentally manipulated intracellular pH (pHi) in normal breast epithelial cells
303 (MCF10A), using inhibitors of the sodium proton exchanger (EIPA) and sodium bicarbonate
304 transporter (S0859) to lower pHi from 7.45±0.12 to 7.10±0.01 and 30 mM ammonium chloride
305 to raise pHi to 8.00±0.27 (**Fig. 3A**). After one hour of pHi manipulation, we assayed for
306 endogenous SHP2 basal activity by immunoblotting for phosphorylation of SHP2 at tyrosine 542
307 (Y542), which is required for activity(*35*). We found that endogenous SHP2 activity is pH
308 sensitive, with increased pY542 levels at low pHi and decreased activity at high pHi compared to
309 control (**Fig. 3B, C**). To investigate downstream signal transduction, we measured SHP2 binding
310 to its signaling-active binding partner, Gab1(*36*) using a co-immunoprecipitation assay. SHP2
311 immune complexes contained significantly more Gab1 when pHi was low compared to control
312 and high pHi (**Fig. 3B, D**). This demonstrates that endogenous SHP2 has pH-dependent activity

in MCF10A cells, with higher activity and binding to the Gab1 signaling partner at low pHi compared to control and high pHi.

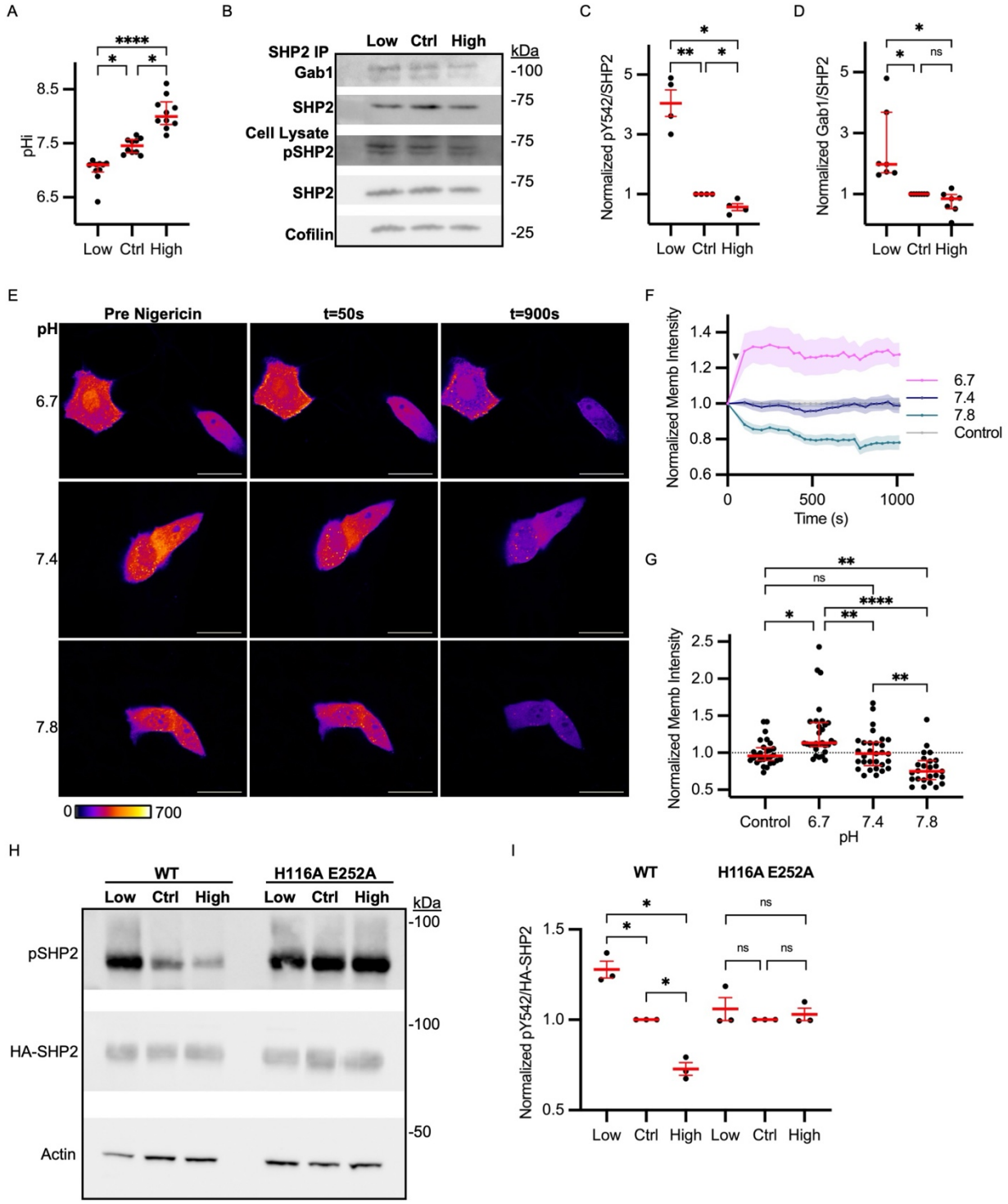

316 ***Figure 3. Intracellular pH regulates SHP2 activity and downstream signaling in MCF10A***
317 ***cells*** (A) pHi measurements of MCF10A cells. Cells were treated with 25 μM EIPA + 30 μM
318 S0858 for 1 hour to lower pH to 7.10. To raise pHi, cells were treated with 30 mM ammonium
319 chloride for 1 hour to raise pH to 8.00. Untreated cells had a pHi of 7.45. Scatter plot shows
320 (median ± interquartile range, N =10) (B) Representative immunoblots of SHP2, Gab1, and
321 phospho-SHP2 (pY542) from SHP2 immune complexes (SHP2 IP) or whole cell lysates (Cell
322 Lysate) isolated from MCF10A cells prepared as in A. (C-D) Quantification of phospho-SHP2
323 (C) and Gab1 Co-IP (D) for replicate data collected as in B. Data was normalized to control in
324 each biological replicate. Scatter plot shows (mean ± SEM, N=4) in C and (median ± IQR, N=7)
325 in D. (E) Representative images of MCF10A cells expressing the SHP2 activity reporter (Grb2
326 TagBFP) pseudocolored on an intensiometric scale. Images show cells prior to manipulating pHi
327 with nigericin buffer (Pre-Nigericin) (see methods for details), 50s after manipulating pHi, and
328 900s after manipulating pHi. Scale bars: 25μm (F) Quantification of images collected as in E.
329 Membrane intensity of SHP2 activity reporter over time was photobleach-corrected and then
330 normalized to initial intensity. Line trace shows (mean ± SEM) from single-cell data (6.7 pH,
331 n=30, 7.4 pH, n=30, 7.8 pH, n=25, control, n=28) collected across N=3 biological replicates. (G)
332 Quantification of endpoint membrane intensities of single cells collected as described in F.
333 Scatter plot shows (median ± interquartile range, N = 5) (H) Representative immunoblot of
334 lysates prepared from MCF10A cells expressing either WT SHP2 or H116A E252A SHP2.
335 Immunoblots show total and pY542-SHP2 under low, control, and high pHi conditions. (I)
336 Quantification of replicate data collected as in H. Scatter plots show (mean ± SEM, N=3).
337 Intensities were normalized to the corresponding control condition. For A and G significance
338 was determined using the Kruskal-Wallis test. For C and I significance was determined using a
339 ratio paired t-test to compare between treatment conditions and a one-sample t-test to compare to
340 control. For D significance was determined using a Wilcoxon test to compare between treatment
341 conditions and a Wilcoxon sign-ranked test to compare to control. * $p<0.05$, ** $p<0.01$,
342 *** $p<0.001$, **** $p<0.0001$.
343

344 We next confirmed the effect of pHi dynamics on basal activity of endogenous SHP2
345 using a live, single-cell reporter of SHP2 activity (tagBFP-Grb2)(*37*). We validated that the
346 tagBFP-Grb2 reporter was robustly recruited to the cell membrane upon EGF stimulation (active
347 SHP2) and that this recruitment was abolished by both a specific SHP2 inhibitor (PHPS)(*38*) and
348 an upstream EGFR inhibitor (Erlotinib) (**Fig. S6A**). We also validated inhibitor efficacy and
349 specificity using western blots to assess EGFR and SHP2 phosphorylation (**Fig. S6B**). Erlotinib
350 treatment reduced EGF-induced pEGFR (pY1068; Grb2 phosphosite) and pSHP2 (pY542),
351 whereas PHPS reduced pSHP2 while leaving pEGFR levels unaffected (**Fig. S6B**). These data
352 show that membrane recruitment of the biosensor is dependent on SHP2 activity.

353 After validating tagBFP-GRB2 as a specific SHP2 activity biosensor, we next measured
354 biosensor recruitment to the MCF10A cell membrane under basal (unstimulated) conditions with
355 and without pHi manipulation using the protonophore nigericin (see methods for details). When
356 the pHi of the MCF10A cells was pinned to 6.7, we observed increased biosensor recruitment to
357 the cell membrane, indicating increased SHP2 activity (**Fig. 3E-G).** Conversely, we observed no
358 change in biosensor recruitment when MCF10A cell pH was pinned to basal pHi conditions (7.4)
359 and reduced biosensor recruitment when the pHi of MCF10A cells was pinned at 7.8 (**Fig. 3F-**
360 **G)**. Importantly, initial biosensor intensity at the membrane was not different prior to nigericin-
361 based pHi manipulation (**Fig. S6C**) and increased biosensor recruitment at low pHi was
362 abolished with the addition of PHPS (**Fig. S6D**). This shows that endogenous SHP2 basal
363 activity is sensitive to pHi dynamics in single living cells.
364 To confirm that the pH sensing network of H116 and E252 mediates pH-dependent SHP2
365 activity in cells, we overexpressed HA-tagged WT SHP2 and SHP2-H116A/E252A in MCF10A
366 cells and quantified SHP2-pY542 levels with and without pHi manipulation. We found that
367 overexpressed WT SHP2 recapitulated the endogenous SHP2 results, with increased activity
368 (SHP2-pY542) at low pHi and decreased activity at high pHi compared to control MCF10A
369 (**Fig. 3H, I**). As expected, the double mutant SHP2-H116A/E252A had pH-independent activity
370 (SHP2-pY524) in MCF10A (**Fig. 3H, I**), confirming that His116 and E252 are required
371 mediators of pH-sensitive SHP2 activity. Through our cell-based analyses, we show that SHP2
372 activity is sensitive to physiological changes in pHi, with increased basal activity at low pHi, and
373 that H116 and E252 mediate pH-dependent activity of SHP2.
374
375

376 **pH sensing nodes cluster at SH2 interface in other SH2 signaling proteins**

377 SH2 domains are modular signaling domains that bind to phosphotyrosine residues,
378 which have experimentally determined pK_as that are close to physiological (5.7-6.1)(*39*, *40*) and
379 are highly structurally and sequence-conserved across signaling proteins(*29*). We hypothesized
380 that networks of residues with physiological pK_as serve a functional role in regulating pH-
381 dependent SH2 binding to phosphotyrosine residues across SH2 domain-containing proteins. To
382 explore this, we applied our in silico computational pipeline to a collection of SH2 domain-
383 containing proteins with multiple solved structures. We found that 90% of SH2 domain-
384 containing proteins tested had ionizable residue networks with pK_as predicted to be shifted into
385 the physiological pH range (**Fig. S7**). As we observed with SHP2, these ionizable residue
386 networks clustered at the SH2 binding interfaces (**Fig. S7**). Interestingly, we observed this
387 pattern of clustering across functional protein classes—finding it in phosphatases (SHP1) (**Fig.
388 S7A**), kinases (ZAP70, JAK1 JAK2, and ABL1) (**Fig. S7B-D, H**), transcription factors (STAT6,
389 STAT5A) (**Fig. S7E-F**), and GTPase activating proteins (CHIO) (**Fig. S7G**).

390 As a control, we also analyzed a collection of SH3 domain-containing signaling proteins.
391 SH3 domains are modular signaling domains that are similarly highly evolutionarily and
392 structurally conserved(*41*), but bind proline-kink regions(*42*) where electrostatics should not
393 drive function. While we identified ionizable networks with physiological pK_as in some SH3
394 domain-containing proteins, the shifted residues did not cluster at the binding interfaces of SH3
395 domains (**Fig. S7H, S7I-K**). This analysis suggests that ionizable networks with upshifted pK_as
396 are not a general feature of all signaling domain interaction interfaces but instead are enriched at
397 functional SH2 domain interfaces.

398

399 **Analysis pipeline applied to Src identifies four networked ionizable residues with predicted**
400 **physiological pK_as**

401 We next selected one of the hits from the screen of SH2 domain-containing signaling
402 proteins (Src) to further validate the role of pH in the allosteric regulation of SH2 domain-
403 containing signaling proteins. The signaling kinase Src has three globular domains: a kinase
404 domain (SH1), an inhibitory SH2 domain that binds phosphotyrosines, and an inhibitory SH3
405 domain that binds proline-rich regions (**Fig. 4A**). The SH2 domain inhibits kinase activity when
406 bound intramolecularly to the C-terminal phosphotyrosine (pY527)(*42*). However, when the SH2
407 and SH3 domains are released, pY527 is dephosphorylated, the activation loop unfurls, and the
408 SH1(kinase) domain autophosphorylates a conserved tyrosine (Y416) in the activation loop (A-
409 loop). Activation loop unfolding and phosphorylation are required for full activation and
410 facilitate Src binding to downstream targets(*42*).

411 We processed seven structures of Src available in the PDB through the computational
412 pipeline. Our analysis identified 5 residues predicted to have physiological pK_as: C185 (pK_a of
413 7.7 ± 0.0), H201 (pK_a of 7.8 ± 0.1), E454 (pK_a of 6.9 ± 0.4), H492 (pK_a of 7.0 ± 0.5), and E524
414 (pK_a of 7.3 ± 0.4) (**Fig. 4B, C**). Four residues (C185, H201, E524, and H492) are networked in a
415 cluster at the interface between the SH2 domain and the kinase domain (**Fig. 4B, C**). E524 is in
416 the C-terminal tail of Src and electrostatically interacts with H201 and C185 in the SH2 domain
417 through bridging glutamate residues (E159, E178) and interacts with H492 in the kinase domain
418 through a bridging aspartate residue (D493) (**Fig. 4B, C**). While E454 has a predicted
419 physiological pK_a, it is in the kinase catalytic site and distant from the SH2 regulatory domain
420 interface (**Fig. 4B**). This analysis of Src again demonstrates that ionizable residue networks with
421 predicted physiological pK_as cluster at SH2 but not SH3 domain interfaces.

A

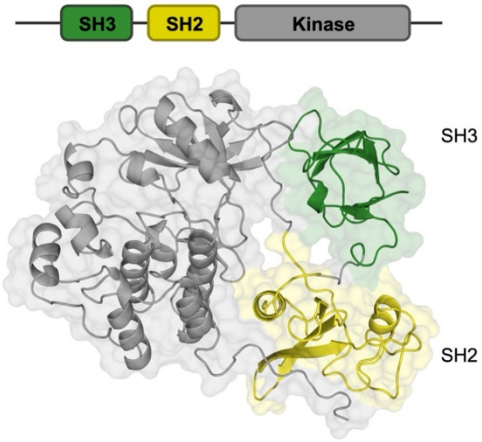

B

Residue	Solution pK_a	Predicted pK_a	Domain
Cys185	9	7.7 ± 0.0	SH2
His201	4.5	7.8 ± 0.1	SH2
Glu454	4.5	6.9 ± 0.4	Kinase
His492	6.5	7.0 ± 0.5	Kinase
Glu524	4.5	7.3 ± 0.4	Kinase

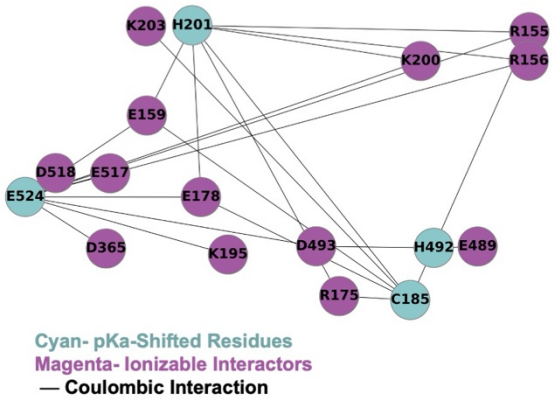

C

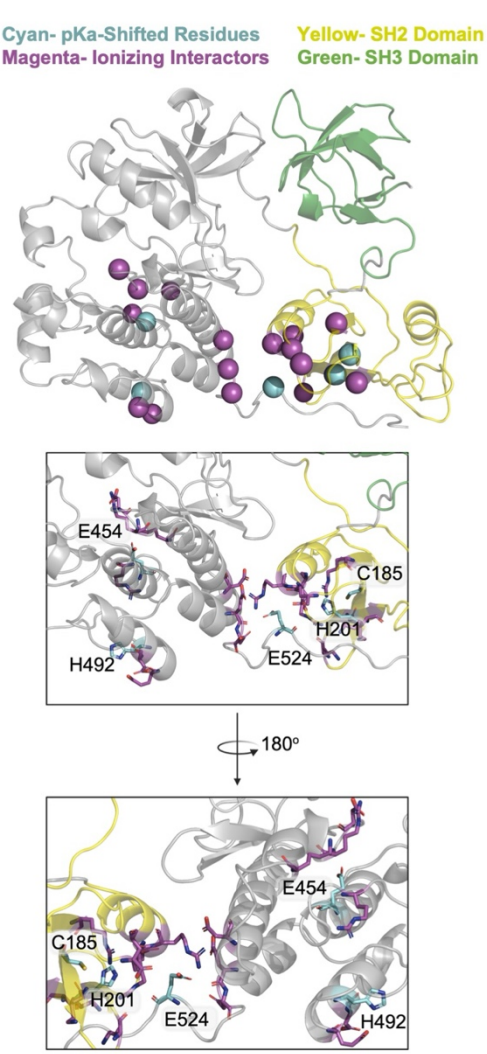

D

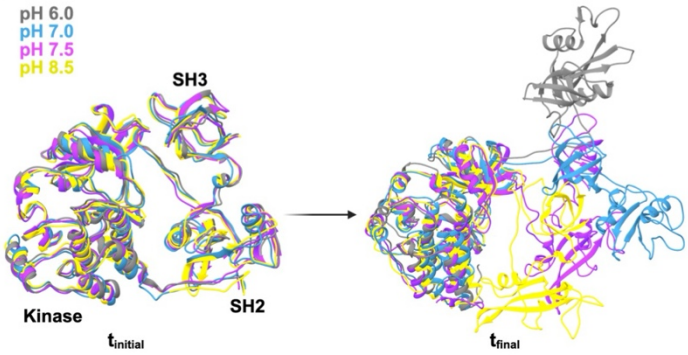

422

423 **Figure 4:** ***Residues with predicted physiological pK$_a$ shifts cluster at the binding interface of***
424 ***the SH2 and kinase domains in Src*** (A) Crystal structure of pilot protein Src shown in cartoon
425 and surface format (PDB ID:2SRC). Kinase domain colored in grey, SH2 domain colored in
426 yellow, and SH3 colored in green (B) Table of predicted pK$_a$s for shifted residues (mean ± SD).
427 Residue interaction network of residues with predicted pK$_a$ shifts (cyan) and their coulombic
428 ionizable interactors (magenta). Edge length reflects the strength of the interaction, with stronger
429 coulombic interactions having shorter edge lengths. (C) Structure of Src (PDB ID:2SRC)
430 showing the kinase domain in grey, SH2 domain in yellow, and SH3 domain in green. Residues
431 identified through in silico ionizable network prediction pipeline shown in spheres. Residues
432 with predicted pK$_a$ shifts (cyan) cluster with ionizable interactors (magenta) across the kinase-
433 SH2 domain interaction interface of Src. Zoom in shows Src structure at the kinase-SH2 domain
434 interaction interface. Networked residues from B and C are shown in stick: residues with
435 predicted pK$_a$ shifts in cyan, interactors in magenta. (D) CpHMD (see methods for details) was
436 performed on Src at pH values from 4.0-10.0. Shown are overlapping views of Src structures at
437 the start of CpHMD simulation (t = 0 ns) and end of simulation (t = 8 ns) for pH values 6.0
438 (grey), 7.0 (cyan), 7.5 (magenta) and 8.5 (yellow).
439

440 We determined the structural conservation of the identified residues in Src and found
441 very high structural conservation of the ionizable network region and individual residues (**Fig.**
442 **S8A-C**). The COSMIC database(*43*) also showed recurrent somatic mutations at each of these
443 sites: C185, H201, H492, and E524 (**Fig. S8D**). Recurrent charge-changing somatic mutations
444 were found in H201, H492, and E524 (Fig S8D, E), suggesting functional importance of the
445 identified network and potential for pH-sensitive network disruption in cancer.
446

447 **CpHMD reveals pH-dependent residue conformations and SH2 domain release in Src**

448 We next assessed pH-dependent structural dynamics in Src using CpHMD (see methods;
449 trajectories in **Movies 14-26**). While we were not able to generate a pK$_a$ for C185 using the
450 CpHMD trajectories (**Fig. S9A**), all other identified residues had upshifted and near-
451 physiological pK$_a$s calculated from the CpHMD trajectories: (H201, pK$_a$ of 7.3; E454 pK$_a$ of 8.2;
452 H492 pK$_a$ of 7.0; E524 pK$_a$ of 6.8) (**Fig. S9B-E**). Local side chain movement showed pH-
453 dependent changes in the identified residue network, suggesting pH-dependent interaction pairs

454 (**Fig S9F, G**). Dihedral angles change with pH for all identified residues, with coupled dynamics
455 observed for connected residues (H201, C185, and H492) between pH 6.5 and 7.5 while E524
456 dihedral angles change at pH values above 7.0 **(Fig S9F**). The CpHMD trajectories also show
457 pH-dependent changes in interdomain interactions between the Src kinase domain and the
458 inhibitory SH2 and SH3 domains (**Fig. 4D**). In agreement with the SHP2 dynamics, the SH2
459 domain of Src was bound more tightly to the kinase domain at high pH (8.5) compared to low
460 pH (6.0), where both the SH3 and SH2 domain were unbound (**Fig. 4D, Movie18**
461 **(2SRC_pH6.0), Movie23 (2SRC_pH8.5)**). We also observed intermediate domain
462 conformations in the pH 7.0 and pH 7.5 trajectories, with Src adopting a conformation where the
463 SH3 domain binds tightly while the SH2 domain is more dynamic (**Fig 4D, Movie20**
464 **(2SRC_pH7.0), Movie21 (2SRC_pH7.5**)). To assess interdomain conformations, we quantified
465 interdomain distances between either the SH2 or SH3 domain and the central kinase domain of
466 Src during the final 3ns of the trajectories. We found pH-dependent SH2-kinase interdomain
467 distances with a maximum (least binding) at pH 6.0 and minimums (tight binding) at high (8.5)
468 and low (4.5) pH (**Fig. S9H)**. We observed similar pH-dependent trends in pH-dependent SH3-
469 kinase interdomain distances, with a maximum (least binding) distance at pH 5.5 and minimums
470 at high (8.5) and low (5.0) pH (**Fig. S9I**). To rule out general pH-dependent structural
471 compaction in these CpHMD trajectories, we also assessed SH3-SH2 domain distances and
472 found no pH dependence (**Fig. S9J**). While these short trajectories are less likely to capture large
473 protein domain movements, the trends across the SHP2 and Src CpHMD analyses are strikingly
474 consistent: low physiological pH (6.0-7.0) leads to SH2 release from the catalytic domain
475 compared to high physiological pH (7.0-8.0) where SH2-catalytic interdomain interactions are
476 increased.

477 **Intracellular pH regulates Src activity and signaling in MCF10A cells**

478 We next determined whether basal kinase activity of endogenous Src is sensitive to
479 physiological pH changes in normal epithelial cells. We assessed Src activity by immunoblot
480 quantification of the levels of pY527, a proxy for inhibited Src, and pY416, a proxy for active
481 Src (**Fig. 5A**). We found that endogenous Src activity was pH sensitive, with increased activity at
482 low pHi compared to control and high pHi (**Fig. 5B-D**) with no change to total endogenous Src
483 levels (**Fig. S10A**). Importantly, the pH-dependent trends in pY527 and pY416 both support the
484 hypothesis that low pHi leads to SH2 domain release, loss of the inhibited Src phosphosite
485 (pY527) (**Fig. 5C**), and gain of the active Src phosphorylation site (pY416) (**Fig. 5D**). Next, we
486 performed immunofluorescence labeling and single-cell analysis of Src activity in MCF10A cells
487 and found that active Src (pY416) was increased at low pHi and decreased at high pHi compared
488 to control cells (**Fig. 5E-G, S10B, C**). We stimulated cells with EGF to determine how pHi
489 regulates Src in the context of growth factor stimulation. We observed significant increases in
490 Src activation (pY416) in EGF stimulated control cells, demonstrating that growth factor
491 stimulation can drive increased Src activation (**Fig. 5E-G**). Interestingly, there was no difference
492 in pY416 levels at low pHi compared to control cells stimulated with EGF, suggesting low pHi
493 phenocopies Src activation via growth-factor stimulation (**Fig. 5E-G**). However, when high pHi
494 cells were stimulated with EGF, activation of Src was lower compared to control cells both with
495 and without EGF stimulation (**Fig. 5E-G, S10B, C**). This indicates that high pH inhibition of Src
496 is sufficient to attenuate the growth factor receptor activation of endogenous Src.

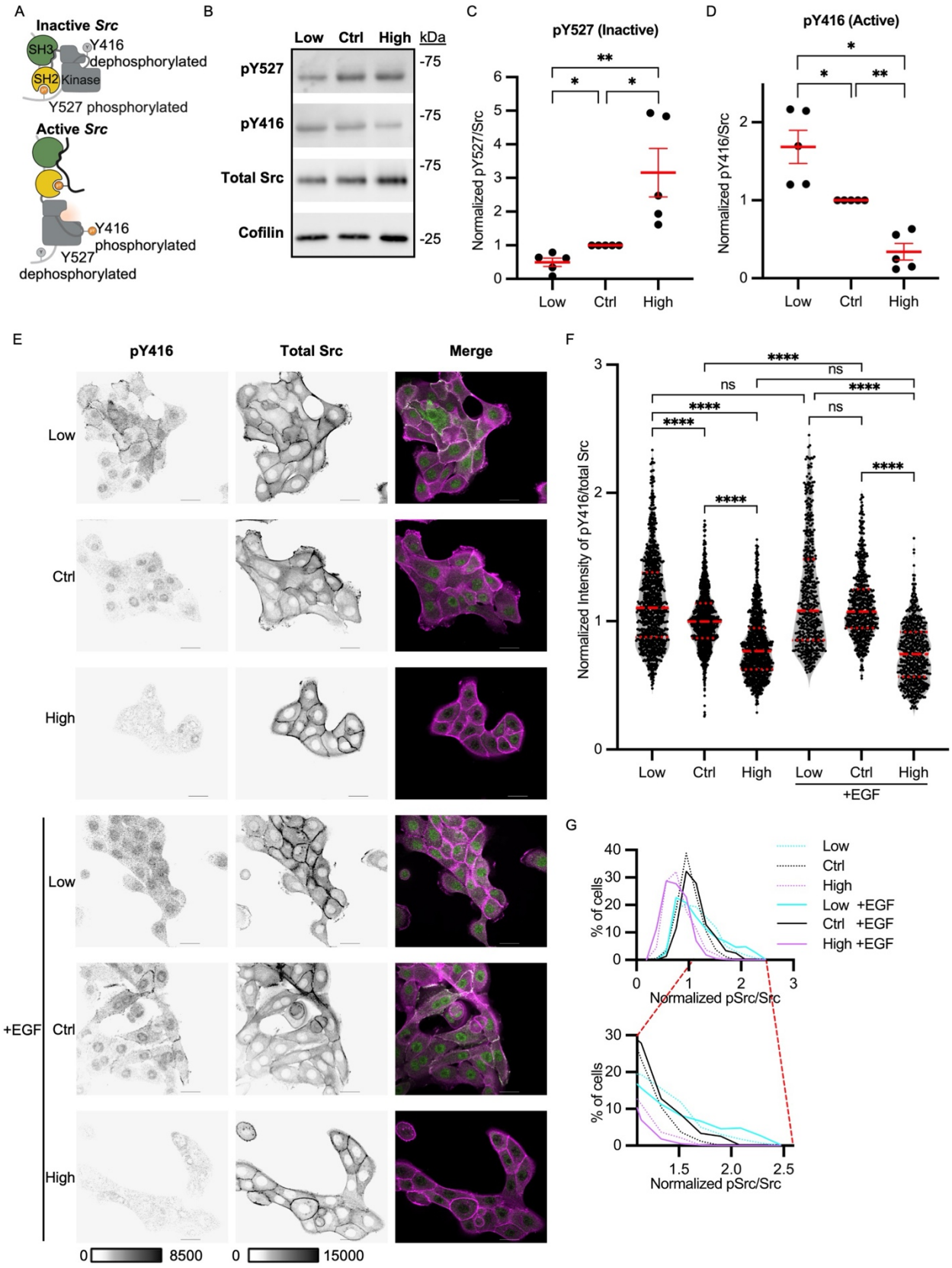
A
Inactive Src
SH3
Y416
dephosphorylated
SH2
Kinase
Y527 phosphorylated
Active Src
Y416
phosphorylated
Y527
dephosphorylated
B
Low
Ctrl
High
kDa
pY527
pY416
Total Src
Cofilin
-75
-75
-75
-25
C
pY527 (Inactive)
Normalized pY527/Src
Low
Ctrl
High
D
pY416 (Active)
Normalized pY416/Src
Low
Ctrl
High
E
pY416
Total Src
Merge
Low
Ctrl
High
+EGF
Low
Ctrl
High
0
8500
0
15000
F
Normalized Intensity of pY416/total Src
Low
Ctrl
High
Low
Ctrl
High
+EGF
ns
****
G
% of cells
Normalized pSrc/Src
Low
Ctrl
High
Low +EGF
Ctrl +EGF
High +EGF

497

498 **Figure 5.** ***Intracellular pH regulates Src activity and localization in MCF10A cells*** (A) Cartoon
499 of Src activation (B) Representative immunoblot from MCF10A lysates prepared from cells
500 maintained for 1 hour at low or high pHi or untreated (control). Immunoblots show total Src and
501 indicated Src phosphorylation sites that reflect protein activation pY527 (inactive) and pY416
502 (active). (C-D) Quantification of pY527 (inactive) (C) and pY416 (active) (D) Src from replicate
503 data collected as in B. Data was normalized to control in each biological replicate. Scatter plots
504 show (mean ± SEM, N=5) (E) Representative confocal images of MCF10A cells fixed and
505 stained for total Src and pY416 (active) Src at given pHi with and without EGF stimulation (10
506 ng/mL for 5 minutes). Total Src and pY416 are shown in inverse mono intensity display. In the
507 merged overlay, total Src is shown in magenta and pSrc is shown in green, areas of high co-
508 localization show white. Scale bar: 25μm. (F) Quantification of single-cell data collected as in E.
509 Levels of pY416 Src are normalized to total Src in each single cell and to control for each
510 biological replicate. Violin plot shows individual cells as points and (median ± IQR, Low,
511 n=984, Control, n=938, High, n=903, Low + EGF, n=525, Control + EGF, n=595, High + EGF,
512 n=599) collected from 6 biological replicates for - EGF conditions and 3 biological replicates for
513 + EGF conditions. (G). Histogram and zoomed in view of single cell data for data shown in F.
514 Low pHi treatment conditions shown in cyan, control in black, and high pHi treatment shown in
515 magenta. For C and D, significance was determined using a ratio paired t-test to compare
516 between treatment conditions and a one-sample t-test to compare to control. For F, significance
517 was determined using the Kruskal-Wallis test. * $p<0.05$, ** $p<0.01$, *** $p<0.001$, **** $p<0.0001$.
518

519 It was at first surprising that growth factor stimulation at low and high pHi did not further
520 increase Src activation (pY416) compared to unstimulated cells with matched pHi (**Fig. 5F**).
521 However, when comparing pY416 Src distributions, we did observe statistically significant
522 differences between EGF stimulated and unstimulated cells across all pHi conditions (**Fig. S10B,**
523 **C**). Our data suggest that pHi manipulation can modulate Src activity in the context of growth
524 factor signaling as well as in basal state.

525 To determine cellular outcomes of pHi-dependent Src activation, we next assessed
526 downstream signal transduction by monitoring downstream activation of ERK (pT202/ pY204)
527 and E-cadherin (pY685). In both cases, pathway activation downstream of Src recapitulated the
528 pH-dependent activity trends, with increased activation at low pHi and decreased activation at
529 high pHi compared to control cells (**Fig. S10D-G**). In control cells, EGF stimulation produced
530 statistically significant increases in downstream activation of ERK (pT202/ pY204) and E-

531 cadherin (pY685) (Fig S10D-G). With EGF stimulation, there was no difference in downstream
532 pathway activation at low pHi compared to control, again suggesting maximal activity is
533 achieved (**Fig. S10D-G**). Finally, high pHi produced lower downstream activation both with and
534 without EGF stimulation compared to matched control conditions (**Fig. S10D-G**). This indicates
535 that low pHi phenocopies EGF stimulation of control cells while high pHi inhibition of Src can
536 attenuate pathway activation even in the presence of extracellular growth factor.
537 To determine whether the identified residue network in Src mediates pH-dependent
538 activity, we overexpressed either FLAG-tagged WT-Src or the quadruple mutant Src-
539 C185A/E454A/H492A/E524A in MCF10A cells. We then quantified pY527 and pY416 levels
540 with and without pHi manipulation by immunoblot. We found that overexpressing WT Src
541 recapitulated the pH-dependent endogenous Src activity results, with decreased phosphorylation
542 of the inhibitory phosphosite (pY527) at low pHi and increased pY527 at high pHi compared to
543 control MCF10A (**Fig. 6A, B**). As with endogenous Src, we also observed pHi-dependent
544 phosphorylation of pY416, with increased active Src (pY416) at low pHi compared to control
545 and high pHi (**Fig. 6A, C)**. Taken together, these data demonstrate that pHi allosterically
546 regulates Src inside cells, with low pHi promoting the active state (pY416, Y527) while high pHi
547 promotes a more inhibited state (Y416, pY527). As expected, the quadruple Src mutant had pH-
548 independent phosphorylation of both pY416 and pY527 while maintaining measurable catalytic
549 activity (**Fig. 6A-C**). Our cell-based analyses show that Src activity is sensitive to physiological
550 pHi changes, with increased activity at low pHi, and that the identified ionizable residue cluster
551 is required for pH-dependent Src activity.
552
553

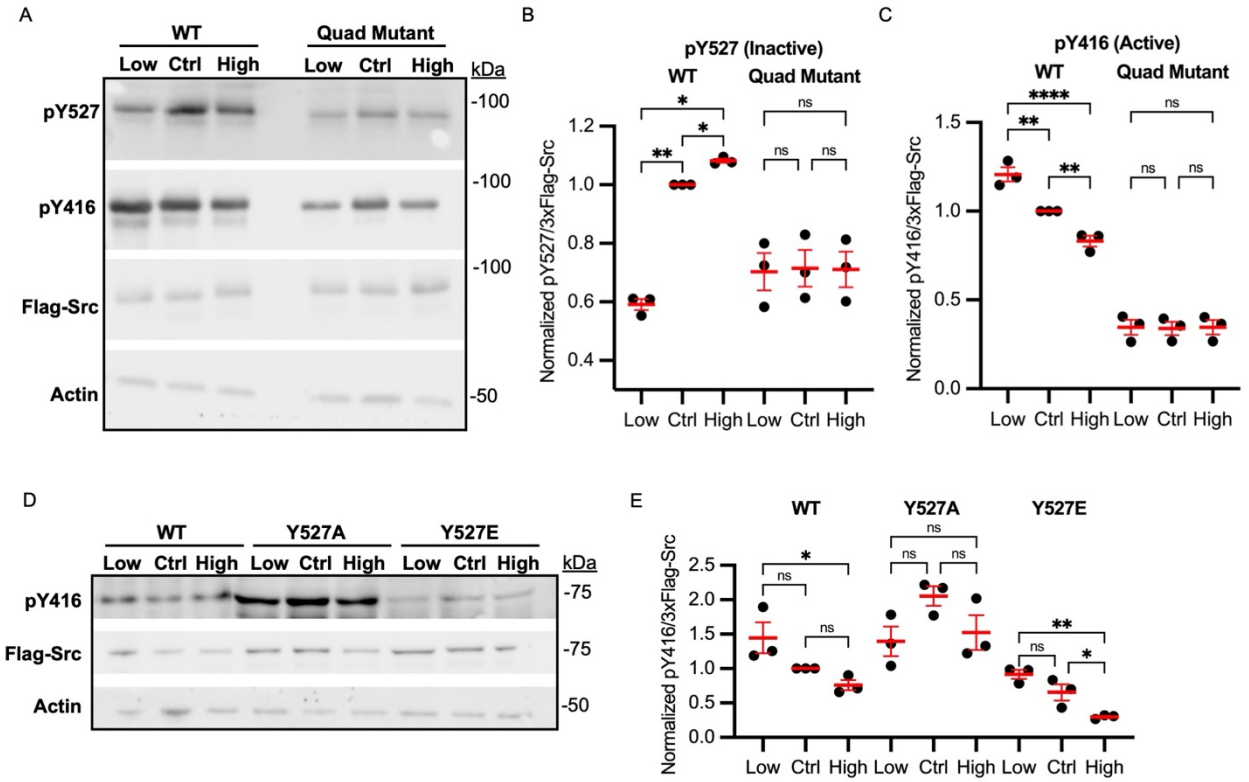

Figure 6. ***Src pH-dependent activity requires an intact ionizable residue network (C185 H201 H492 E524)*** (A) Representative immunoblot from MCF10A lysates expressing either WT Src or the Quad Mutant (Src- C185A/H201A/H492A/E524A) and maintained for 1 hour at low or high pHi or untreated (control). Immunoblots show total Src and indicated Src phosphorylation sites that reflect protein activation pY527 (inhibited) and pY416 (active). (B) Quantification of pY527 (inactive) from replicate data collected as in g. Data was normalized to control in each biological replicate. Scatter plots show (mean ± SEM, N=3) (C) Quantification of pY416 (active) from replicate data collected as in g. Data was normalized to control for each biological replicate. Scatter plots show (mean ± SEM, N=3) (D) Representative immunoblot from MCF10A lysates expressing either WT Src, Y527A Src, or Y527E Src and maintained for 1 hour at low or high pHi or untreated (control). Immunoblots show total Src and indicated active Src phosphorylation site (pY416). (E) Quantification of pY416 (active) from replicate data collected as in D. Data was normalized to WT control for each biological replicate. For B and C, significance was determined using a ratio paired t-test to compare between treatment conditions and a one-sample t-test to compare to WT control. For E, significance was determined using a one-way ANOVA and a one-sample t-test to compare to WT control. * $p<0.05$, ** $p<0.01$, *** $p<0.001$, **** $p<0.0001$.

To further probe contributions of individual residues in the identified residue network to pH-sensitive Src activity, we generated single point mutants (Src-C185A, Src-E524A, Src-H201A, and Src-H496A) and measured their activity in MCF10A cells. First, we found that the

576 E524A mutant pushed Src into a more active, but still pH-dependent, state: Y527 was
577 significantly dephosphorylated compared to WT Src and pH-independent while Y416
578 phosphorylation was still pH-dependent but increased compared to WT (**Fig. S11A-C**). This
579 suggests E524 is required for the observed pH-dependence of pY527 in wild-type Src: without
580 E524, affinity for pY527 is reduced and the Src C-terminal tail release from the SH2 domain is
581 pH-insensitive in the physiological range. We can also conclude from the E524A data that the
582 remaining residue network (C185, H201, and H495) is sufficient to preserve pH-dependent
583 phosphorylation of active-loop residue (Y416) (**Fig. S11A-C**).

584 We found that C185A and H496A still exhibited trends of pH-dependent phosphorylation
585 of both Y527 and Y416 (**Fig. S11A-F**), suggesting C185 and H496 are not essential for either
586 pH-sensitive phosphorylation event on Src. However, because we cannot easily titrate across
587 wider pHi ranges in these cells (e.g. 6.1-8.0), we cannot rule out the possibility that C185 and
588 H496 may be critically important for tuning the pKa of the entire residue network. Finally, the
589 H201A mutant locked Src into an inhibited and pHi-independent conformation, with
590 significantly reduced Y416 phosphorylation compared to WT (**Fig. S11D-F**). This suggests
591 H201 plays a predominant role in regulating the pH-dependent active-loop phosphorylation of
592 Y416 observed in both WT and Src-E524A.

593 Finally, to determine the specific role pH plays in regulating the well-characterized (*44*,
594 *45*)phospho-tyrosine activation of Src, we assessed pH-dependent Src activity with Y527
595 phosphomimetic mutants. We mutated Y527 to a non-titrating alanine that mimics a
596 constitutively dephosphorylated Y527 and to a titratable glutamate that mimics a constitutively
597 phosphorylated Y527. As expected, Src-Y527A was constitutively active (high pY416) and pH-
598 independent (**Fig. 6D,E**). This data phenocopies Src constitutive activation when Y527 is

599 mutated or deleted (*44*). Conversely, we found that Src-Y527E activation was still pH dependent,
600 with higher activity at low pHi and lower activity at high pHi when compared to control (**Fig.**
601 **6D,E**). Taken together, these data suggest phosphorylation of Y527 contributes to the
602 modulation of pH-dependent wild-type Src activation. Thus, our data suggest pHi dynamics
603 function as a rheostat to modulate WT Src activity in concert with traditional modes of Src
604 regulation (phosphorylation).
605

606 **Discussion**

607 Our data show that our in silico analysis pipeline can be used to predict and
608 mechanistically probe pH-dependent protein function. We applied this analysis to characterize
609 molecular mechanisms of pH-dependent allostery for the known pH sensor SHP2 (**Fig. 7A**). We
610 find that physiological changes in pHi (0.1-0.4 pHi units) can produce 2-3 fold changes in basal
611 SHP2 activity. We also used our computational pipeline to identify novel pH regulation of Src
612 activity and identify the critical pH sensing residues (**Fig. 7B**). Importantly, we showed that the
613 pH sensitive regulation of Src functions in concert with the well-characterized mode of
614 phosphorylation (pY527) regulation. For example, simply lowering pHi can phenocopy Src
615 activation growth factor stimulation and low pH can activate Src even when a phosphomimetic
616 auto-inhibitory mutant is used (Src-Y527E). These data suggest that the transient pHi dynamics
617 previously reported during cell cycle progression (0.1-0.2 pH units) (*2*, *46*), cell migration (~0.3
618 pH units) (*4*, *47*, *48*) and cell differentiation (~0.4 pH units) (*49*) may be sufficient to regulate
619 basal cell signaling state of SHP2 and Src.

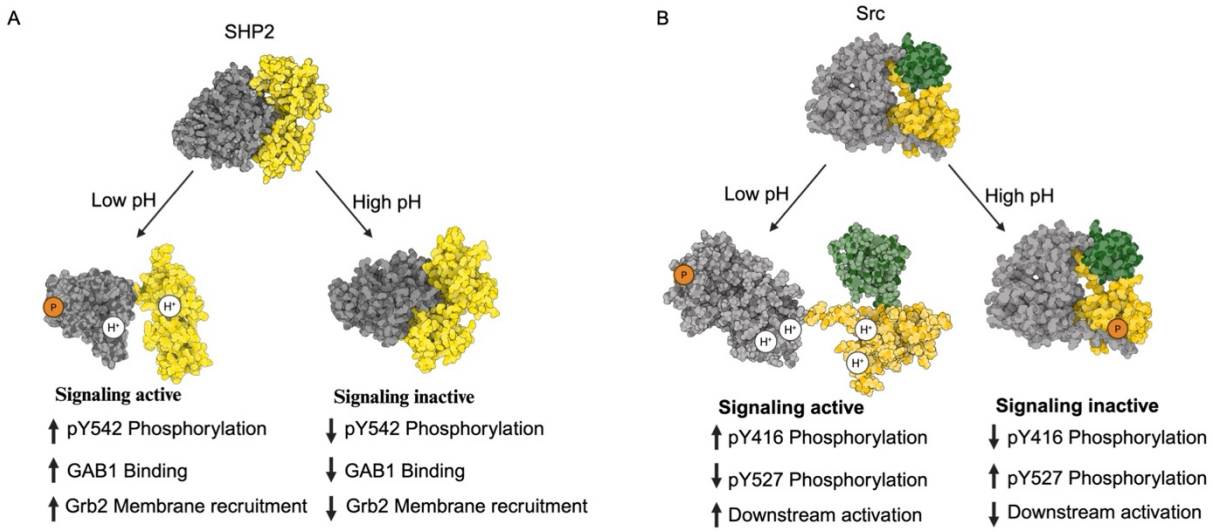

Figure 7. ***Molecular mechanism of pH-dependent allostery of SHP2 and Src*** (A) Schematic of pH-driven activation and inhibition of SHP2. At low pH, the SH2 domain is unbound and SHP2 becomes signaling active with increased phosphorylation of Y542, increased GAB1 binding, and increased Grb2 recruitment. (B) Schematic of pH-driven activation and inhibition of Src. At low pH, the SH2 domain is unbound and Src becomes signaling active with increased phosphorylation of Y416, decreased phosphorylation of Y527, and increased substrate phosphorylation and downstream activation.

We also demonstrated that ionizable residues with predicted physiological pK_as are conserved across many SH2 domain-containing signaling proteins including kinases, phosphatases, transcription factors, and GTPase activating proteins. For multi-functional proteins that contain both evolutionarily conserved SH2 and SH3 domains, the residue networks with predicted physiological pKas clustered specifically at the interfaces between SH2 and the functional domains. This suggests that SH2 domains may be primed for pH sensitive allosteric regulation of signaling proteins. Our data showing the pH-dependence of Src under growth factor stimulation in cells and when using phosphomimetic mutants also suggests that pH-dependent regulation of SH2 signaling proteins may function in concert with traditional growth factor

638 signaling and phosphorylation-dependent regulation. Future work will expand on this hypothesis
639 with more mechanistic detail and functional validation.

640 We show that our prediction pipeline is as accurate as more computationally expensive
641 prediction methods and does not require crystallographic waters or paths to solvent to identify
642 residue networks. Our pipeline is also modular, enabling incorporation of improved pK_a
643 prediction algorithms (e.g. recent machine learning (ML) pipelines with improved accuracy over
644 PROPKA)(*50*). Most characterized pH-sensitive proteins have simple mechanisms where a
645 single histidine residue titrates with changes in pH to confer changes in protein structure and
646 function. We applied our network analysis to accurately identify previously validated pH-sensing
647 residues based on existing structures, including in mutant p53 (His273)(*51*) and the sodium
648 proton exchanger (H544)(*52*) (**Fig. S12**). We also showed that our pipeline accurately identified
649 one of the only validated complex multi-site pH sensing mechanisms in isocitrate dehydrogenase
650 1 (D273, E304, K217)(*53*) (**Fig. S12**) this network was first reported using the more
651 computationally expensive pHinder program to predict residues with physiological pKas (*53*).
652 Interestingly, recent work has suggested that His242 is required for pH-sensitive activity of
653 phosphofructokinase muscle isoform (PFKM), but mutation of this residue did not completely
654 abrogate the pH sensitive activity of PFKM (*54*). Our network analysis indicates that PFKM has
655 two networked residues with physiological pKa (His242 and Asp309) (**Fig. S12**) and suggests
656 that mutating both residues may fully abrogate pH-dependent PFKM function.

657 Scientists can apply our in silico approach to improve our mechanistic understanding of
658 pH-dependent cell behaviors lacking known pH-sensitive molecular drivers, including
659 differentiation(*49*, *55*), cell cycle progression(*2*, *3*), and epithelial to mesenchymal transition(*56*,
660 *57*). In addition to revealing the pH-dependent structural proteome, this approach can be applied

661 to molecularly characterize how dysregulated pHi drives pathophysiology in cancer (increased
662 pHi)(*6*, *58*) and neurodegeneration (decreased pHi)(*59*).
663

664 **Materials and Methods**

665 **pK_a prediction method**

666 All full-length structures for proteins of interest were first identified based on the gene search
667 and downloaded from the Protein Database (https://www.rcsb.org/). Next, the electrostatic
668 properties for each structure were calculated using the APBS (Adaptive Poisson-Boltzmann
669 Solver) webserver (https://server.poissonboltzmann.org/). The APBS calculation was performed
670 using the following parameters: The pH for continuum electrostatic calculations was set to 7.4.
671 The AMBER forcefield was used for the minimization step. We set the parameters in the APBS
672 webserver to ensure that new atoms were not rebuilt too close to existing atoms and that
673 hydrogen bonding networks were optimized during the structure repair and refinement step. The
674 electrostatic data for each individual structure was combined into a single dataset and ionizable
675 residues were then filtered for physiologically relevant pK_as. Histidine residues with pK_as above
676 7.0 were considered physiologically relevant while aspartates, glutamates, and lysines were
677 filtered if pK_as were between 6.8.00. For ionizable residues that were classified using these
678 criteria as "shifted" in ≥ 50% of structures, residue pK_as were averaged across all structures in
679 the dataset. Next, the strength of coulombic interactions for the shifted residues were averaged
680 for all structures. Structural visualization was done using Pymol and residue interaction networks
681 were generated in Python (https://zenodo.org/records/15338058). For residue interaction
682 networks, the length of the connecting lines indicates the strength of the coulombic interactions,
683 with stronger coulombic interactions having shorter vectors.

684

685 **pK_a prediction benchmarking**

686 A diverse set of experimental pK_a values were collected for Asp, Glu, His, Tyr and Lys from
687 previous studies (*17*). The experimental dataset contained 34 proteins with 290 experimentally
688 determined pK_as. Using our pipeline, we calculated the pK_as of these previously determined
689 ionizable residues. We then calculated the weighted correlation coefficient for then predicted
690 pK_as against the experimental pK_as and the Root Mean Squared Deviation (RMSD) of the
691 predicted pK_a from the experimental values. The Garcia-Moreno lab have also calculated far-
692 shifted pK_as for ionizable residues in Staphylococcal nuclease (SNase) (*18–20*). To determine if
693 our pipeline was able to accurately predict these large pK_a shifts, we also generated a dataset
694 comparing the delta pK_as of the validated dataset against our predictive set and calculated
695 correlation coefficients and RMSDs from the experimental values.

696

697 **Structural conservation**

698 The ConSurf server was used as a bioinformatics tool to estimate evolutionary conservation in
699 proteins of interest. To determine the evolutionary conservation in our proteins of interest, we
700 followed the recommended guidelines outlined by Yariv *et al.*, 2023(*33*). Briefly, the SHP2
701 (PDB: 2SHP) and Src (PDB:2SRC) protein structures were submitted to the ConSurf Web server
702 (https://consurf.tau.ac.il/). ConSurf server utilizes an empirical Bayesian algorithm for
703 conservation scores ranging from 1 to 9; where 1 is variable and 9 is conserved.

704

705

706

707 **Purification of SHP2 proteins**

708 Full-length SHP2 variants were cloned into the pGEX-4TI SHP2 WT plasmid(*60*), pGEX-4T1
709 SHP2 WT was a gift from Ben Neel (Addgene plasmid # 8322 ; http://n2t.net/addgene:8322 ;
710 RRID:Addgene_8322)) and expressed in *E. Coli* for purification. Transformed BL21(DE3) cells
711 were grown in Miller's Modified Luria Broth (RPI, L24080-2000) supplemented with 0.1
712 mg/mL ampicillin at 37°C with shaking (250 rpm). When cells reached an OD600 of 0.6,
713 proteins were induced with Isopropyl β- d-1-thiogalactopyranoside (IPTG) (Thermo Scientific,
714 R0392) (0.42 mM) and incubated at 18°C overnight with shaking (250 rpm). The induced
715 cultures were centrifuged at 10,000 rpm at 4°C for 30 mins and resuspended in lysis buffer (B-
716 PER™ Bacterial Protein Extraction Reagent (Thermo Scientific, 78243)) supplemented with
717 EDTA-free Protease Inhibitor Cocktail (Roche, 04693132001)). Cell lysates were placed on a
718 rocker at 4°C for 10 mins before centrifugating at 40,000 rpm at 4°C for 40 minutes. The
719 supernatant was separated, and glutathione resin (GenScript, L00206) was added to bind the
720 GST tagged proteins. The mixture was rocked for an hour at 4ºC and then purified in a
721 CrystalCruz chromatography column (Santa Cruz, sc-205554) at 4°C. Purified proteins were
722 dialyzed into dialysis buffer (20mM Tris 50mM NaCl 1mM DTT 5% glycerol, pH 7.5) overnight
723 at 4°C and stored at -20°C.

724

725

726 **Phosphatase activity assays**

727 SHP2 variants were quantified by measuring absorbance at 280 nm and comparison with BSA
728 protein standards. Para-nitrophenyl phosphate (pNPP) (Thermo Scientific, 34045) was used as an
729 artificial substrate for the protein tyrosine phosphatase (PTPase) activity of each SHP2 variant.

730 Reactions were performed at 30°C in 100 µl volume of PTPase buffer (25 mM Tris–HCl, 50 mM
731 NaCl, 2 mM EDTA and 10 mM dithiothreitol). Concentrations of pNPP ranged from 12-400 mM
732 (12, 15.6, 25, 31.2, 50, 62.5, 100, 125, 250, 300, 400) and assay buffer pH values ranged from
733 6.1 to 8.0. All assay conditions were performed in technical duplicates in 96-well plates.
734 Reactions were initiated by the addition of 5µg of WT or mutant SHP2 to the reaction mixtures.
735 Kinetic absorbance readings were collected at 405 nm over 30 mins on a spectrophotometer
736 (Biotek Cytation 5). In all cases, after averaging technical replicates, the linear region of the
737 reaction progress curve was determined by visual inspection and fit to a slope against the time of
738 progression. These slopes were then plotted against the corresponding concentrations of substrate
739 and fit to the Michaelis-Menten equation using non-linear regression to determine catalytic
740 parameters. Experiments were repeated at least three times across two batches of purified
741 proteins, and the average and standard error of the mean for all biological replicates are reported.
742
743 **Cell culture**
744 Normal breast epithelial MCF10A cells were grown in complete media: DMEM/50% F12 w/
745 GlutaMax (Invitrogen, 10565-018) supplemented with 5% Horse Serum (Invitrogen, 16050-
746 122), 0.02 µg/mL EGF (Peprotech, AF-100-15), 5 µg/mL Hydrocortisone (Sigma, H-0888), 10
747 mg/mL Insulin (Sigma, I-1882), 0.1 µg/mL Cholera toxin (Sigma, C-8052), and 1% Penicillin-
748 Streptomycin (Corning, 30-001-Cl). Cells were maintained in humidified incubators at 37°C
749 with 5% CO_2. MCF10A cells (ATCC: CRL-10317) were split at sub-confluency. Cells were
750 monitored for maintenance of epithelial morphology throughout experimental protocols. To
751 lower pHi, complete media was supplemented with 25 µM EIPA (Invitrogen, E3111) and 30 µM
752 S0859 (Sigma-Aldrich, SML0638-5MG). To raise pHi, complete media was supplemented with

753 30 mM ammonium chloride (NH_4Cl, Fisher Chemical, A661-500, Lot 185503). To inhibit SHP2,
754 complete media was supplemented with 15 μM PHPS1(Sigma-Aldrich, P0039) for 1 hour. To
755 inhibit EGFR, complete media was supplemented with 1 μM Erlotinib (BioVision, 1588-1000)
756 for 1 hour. To stimulate EGFR signaling, media was spiked with 10 ng/mL EGF (Preprotech,
757 AF-100-15-100UG) for 5 mins. All chemical concentrations are final concentrations (Cf).
758
759 **pHi Manipulation and measurement**
760 MCF10A cells were plated in 6 technical replicates for each treatment condition (6×100,000
761 cells/well; 24 well plate; 1 mL total volume). 24 hours after plating, media was exchanged with
762 pHi manipulation media. After 1 hour of incubation with pHi manipulation media, pHi was
763 measured as previously described(*61*). Briefly, 2′,7′-Bis-(2-Carboxyethyl)-5-(and-6)-
764 Carboxyfluorescein, Acetoxymethyl (BCECF-AM) Ester (Biotium, 51011) was added at 2 μM
765 (Cf) to cells for 30 min at 37°C with 5% CO_2. Cells were then washed 3x5 min with HEPES-
766 based wash buffer (30 mM HEPES, 145 mM NaCl, 5 mM KCl, 10 mM glucose, 1 mM KPO_4, 1
767 mM $MgSO_4$, and 2 mM $CaCl_2$) at 37°C. Wash buffers were supplemented with appropriate pH-
768 altering compounds at the same concentrations as the media. After washes, kinetic fluorescence
769 measurements were made at pH-sensitive wavelengths (490ex/535em) and the pH-insensitive
770 wavelengths (440ex/535em) every 15sec for 5 minutes at Medium PMT sensitivity on a plate
771 reader (Biotek Cytation 5). After the initial kinetic pHi read, wash buffers were removed and
772 replaced with the isotonic standardization buffer at ~7.5 pH (25 mM HEPES, 80 mM KCl, 1 mM
773 $MgCl_2$) supplemented with the protonophore nigericin (Invitrogen, N1495) at 10 μM (Cf). Cells
774 were incubated at 37°C for 10 min, and the plate was read again with the same parameters. The
775 high pH standardization buffer was then replaced with a ~7.0 pH nigericin buffer standard, cells

776 were incubated at 37°C for 10 min, and the plate was read again with the same parameters. The
777 nigericin buffer was then replaced with a ~6.5 pH nigericin buffer standard, cells were incubated
778 at 37°C for 10 min, and the plate was read again with the same parameters. Mean intensities
779 from pHi measurement and the nigericin standards were exported and pHi was back calculated
780 using a nigericin linear regression performed on each well with Nigericin standard pHi reported
781 to the hundredths place.
782
783 **Western blotting**
784 After pHi manipulation plates were removed from the incubator and placed on ice. The media
785 was aspirated, and the plates were washed two times with ice-cold DPBS. 200µL of lysis buffer
786 (500 mM NaCl, 10 mM EDTA, 500mM HEPES-free acid, 10 mM EGTA, 10% Triton X-100,
787 protease inhibitor cocktail (Pierce™ Protease Inhibitor Tablets, A32965; 1 tablet/50 mL lysis
788 buffer) and phosphatase inhibitor cocktail (PhosSTOP™, Sigma Aldrich, 4906845001), (pH 7.4)
789 was added to each plate. After 15 minutes of incubation in the lysis buffer, cells were removed
790 using cell scrapers and transferred to pre-chilled microfuge tubes. Lysates were centrifuged at
791 14,000 x g for 15 minutes at 4°C. Clarified lysates were isolated to separate microfuge tubes on
792 ice. The Bradford assay was used to quantify the total protein content of lysates (Bradford, 1976)
793 using Coomassie Protein reagent (Thermo Scientific, cat: 1856209). Lysates were stored at -
794 80°C if not immediately being used for SDS-PAGE sample preparation.
795
796 Protein samples were prepared in 6X Laemilli (reducing) buffer (Thermo Scientific, J61337-AC)
797 and boiled for 5 minutes at 100°C. A total of 10 µg of MCF10A lysate was added to each lane
798 for immunoblot analysis. Protein samples were loaded onto 12% SDS-PAGE gels, which were

799 run at 175V and 0.08 Amps for 15 minutes to stack samples. Protein samples were separated by
800 running the gel at 200 V and 0.08 Amps for an hour and a half. Polyvinylidene difluoride
801 (PVDF) membranes were pre-soaked in 100% methanol for 5 minutes and rinsed in turbo
802 transfer buffer. Transfers were performed at 1.00 A and 25V for 30 mins using the TransBlot
803 Turbo Transfer System (BioRad). Membranes were blocked for 1 hour in 5% milk (or 5% BSA
804 for phospho-proteins) in 1X Tris-buffered Saline + 0.1% Tween® 20 (TBS-T) at room
805 temperature with shaking. Membranes were washed 3x5 min in 1X TBS-T before being cut and
806 incubated with primary antibodies. The following primary antibodies were used: SHP2 (Cell
807 Signaling Technology, 3752; 1:1000 dilution in 1% milk in 1X TBS-T), pSHP2(Tyr524) (Cell
808 Signaling Technology, 3751T; 1:1000 dilution in 1% BSA in 1X TBS-T), Cofilin (Cell
809 Signaling Technology, 5175; 1:1000 dilution in 1% milk 1X TBS-T), HA (Cell Signaling
810 Technology, 3724; 1:1000 dilution in 1% milk 1X TBS-T), Actin (Santa Cruz, sc58673; 1:1000
811 diluted in 1% milk in 1X TBS-T), Src (Cell Signaling Technology, 2109; 1:1000 dilution in 1%
812 milk 1X TBS-T), pSrc(Tyr527) (Cell Signaling Technology, 2105; 1:1000 dilution in 1% BSA in
813 1X TBS-T), pSrc(Tyr416)(Cell Signaling Technology, 6943; 1:1000 dilution in 1% BSA in 1X
814 TBS-T), ERK (Santa Cruz, sc-514302; 1:1000 diluted in 1% milk in 1X TBS-T), pERK (Cell
815 Signaling Technology, 4370S; 1:1000 dilution in 1% BSA in 1X TBS-T), E-cadherin (Fisher
816 Scientific, 13-190-0; 1:1000 diluted in 1% milk in 1X TBS-T), pE-cadherin (ThermoFisher
817 Scientific, PA5-143661, 1:1000 diluted in 1% BSA in 1X TBS-T). Primary antibodies were
818 incubated overnight at 4°C with shaking. Primary antibody solutions were removed, and
819 membranes were washed 3x5 minutes in 1X TBS-T before incubating secondary antibodies
820 (Goat anti-mouse/rabbit HRP-conjugated antibodies; 1:10,000 diluted in 1% milk/BSA in 1X
821 TBS-T) for 1 hour at room temperature with shaking. Secondary antibody solutions were

822 removed, and membranes were washed 3x5 minutes in 1X TBS-T before being developed using
823 Pierce SuperSignal West Pico PLUS (Thermo Scientific, 34580) or Pierce SuperSignal West
824 Femto PLUS (Thermo Scientific, 34095). Chemiluminescence and colorimetric images were
825 acquired using a BioRad ChemiDoc imager.
826
827 Raw files were exported from ChemiDoc imager and opened in ImageJ. Band intensities were
828 acquired by densitometry analysis (area under the curve of individual bands in respective lanes).
829 For each replicate blot, target protein intensities were normalized to the intensity of loading
830 controls before normalizing each condition ratio to that of the control within biological
831 replicates.
832
833 **Co-immunoprecipitation assays**
834 After pHi manipulation plates were washed 2x with ice-cold PBS. The cells were then lysed on
835 ice. After Bradford measurements, 1µg of anti-SHP2 (Rabbit, Cell Signaling, 3752) was added to
836 100 µg of total lysate. The mixture was incubated on the rocker overnight at 4°C. Next, 80 µl of
837 protein A-dynabeads were added to each tube and the mixture was incubated on the rocker for 4
838 hours at 4°C. Next the beads were washed 3 times with 800 µl of wash buffer (TBS + 0.1%
839 Tween, EDTA-free Protease Inhibitor Cocktail (Roche, 04693132001)). After the final wash, the
840 beads were heated at 50°C in 50 µL of 2x Laemilli sample buffer (Biorad, 1610737) for 5
841 minutes to elute the proteins. Next the immunoprecipitation samples and total lysates were
842 immunoblotted. The following antibodies were used for primary incubations: SHP2(abcam,
843 ab76285; 1:1000 dilution in 1% milk in 1X TBS-T), GAB1 (Santa Cruz Biotechnology, sc-
844 133191, 1:1000 dilution in 1% milk in 1X TBS-T).

845

846 **GRB2 TagBFP Assay: Live-cell Microscopy**

847 The pHR Grb2-TagBFP plasmid, a gift from Jared Toettcher (Addgene plasmid # 188631
848 ; http://n2t.net/addgene:188631 ; RRID:Addgene_188631)(*37*), was transfected into MCF10A
849 cells and grown for 24 hours before plating for experiments. The cells were plated on a 35mm
850 imaging dish with a 14mm glass coverslip (Matsunami, D35-14-1.5-U) a day before imaging.
851 Cell membranes were visualized via CellMask Deep Red (Thermo Fisher, C10046; 1:20,000),
852 incubated for 10 mins at 37°C in complete media. Microscope objectives were preheated to
853 37°C, and the stage-top incubator was preheated to 37°C and kept at 5% CO_2/95% air. Confocal
854 images were collected on a Nikon Ti-2 spinning disk confocal with a 60× (CFI PLAN FLUOR
855 NA 1.3) oil immersion objective. The microscope is equipped with a stage-top incubator (Tokai
856 Hit), a Yokogawa spinning disk confocal head (CSU-X1), four laser lines (405 nm, 488 nm, 561
857 nm and 647 nm), appropriate filter sets (BFP: 455/50; GFP: 525/36; Tx red: 605/52, and Cy5:
858 705/72), a Ti2-S-SE motorized stage, multi-point perfect focus system and an Orca Flash 4.0
859 CMOS camera. The cells were imaged initially for starting intensities before nigericin
860 stimulation. Next, the media was replaced with nigericin buffer (see **pHi manipulation and**
861 **measurement** section) to pin the cells at different pH values. The BFP (405 ex, 455/50 em;
862 500ms exposure) and Cell Mask (647ex, 705/72 em; 300ms exposure) for 15 mins at 30 second
863 intervals. The image quantification was performed in Nikon Elements software. Images were
864 background-subtracted using a region of interest (ROI) drawn on a glass coverslip (determined
865 by DIC). To only measure the intensity of the cell membrane, the ROI for membrane of each cell
866 was outlined using the membrane marker and tracked over time. In case of improper tracking
867 over time points, manual tracking was used to redraw ROIs.

868

869 **Immunofluorescence assays**

870 MCF10A Cells were plated in 35mm imaging dish with a 14mm glass coverslip
871 (Matsunami, D35-14-1.5-U) a day before treatment. The cells were then treated with pHi
872 manipulation drugs for an hour. Cells were rinsed with DPBS and fixed in 3.7% formaldehyde
873 (Alfa Aestar, 33314) at room temperature for 10 min. Cells were washed three times for 2 min
874 each time with DPBS, then incubated in lysis buffer (0.1% Triton-X in DPBS) for 10 min at
875 room temperature. Cells were washed three times for 2 min each time with DPBS, then
876 incubated in blocking buffer (1.0% BSA in DPBS) for 1 hour at room temperature with rocking
877 followed by three 2 min washes in DPBS. Cells were then incubated overnight at 4°C with anti-
878 C-Src antibody (Proteintech, 60315-1-Ig) and anti-pY416-C-Src antibody (ThermoFisher
879 Scientific, 44-660G). Cells were washed three times for 3 min each time in DPBS, then
880 incubated with secondary antibody and phalloidin for 1 hour at room temperature. After three 3
881 min washes in DPBS, Hoechst 33342 dye (1:20,000) in antibody buffer was added for 10 min,
882 then removed. Cells were imaged in DPBS on the spinning disk confocal microscope. Images
883 were collected in BFP (405 nm laser excitation, 455/50 nm emission, 200-500msec exposures);
884 GFP (488 nm laser excitation, 525/36 nm emission, 200-500msec exposures); Tx red (561 nm
885 laser excitation, 605/52 nm emission, 200-500msec exposures); and Cy5(647 nm laser excitation,
886 705/72 nm emission, 200-500msec exposures).

887 **Constant pH molecular dynamics**

888 The 2SHP and 2SRC monomer chains were downloaded from Protein Data Bank (PDB)
889 for initial structures. Constant pH MD (CpHMD) simulations were conducted following the
890 protocol described by Henderson *et al*., 2022(*34*). CpHMD simulations were performed with

implicit solvent using the GBNeck2-CpHMD method implemented in AMBER 2022(*62*). Preparation of input files was done using the cphmd_pred.sh script provided in the protocol(*34*), using the default titratable residue types (Asp, Glu, His, Cys, Lys). After energy minimization, structure relaxation, and protonation state initiation(*34*), independent production simulations were run over 4.0-10.0 pH in half-integer increments for 8 nanoseconds (ns) for each, resulting in 13 independent CpHMD simulations and 104 ns of total simulation time for each structure. Coordinate snapshots were saved every 20 picoseconds (ps), and protonation state snapshots every 2 ps. The probability of protonated states became time-independent after 4 ns. The resulting coordinate and protonation state trajectories were analyzed using Python scripts provided in the protocol(*62*), the CPPTRAJ analysis program(*63*), and in-house Python scripts (https://zenodo.org/records/15338058). To create the initial structure for the H116AE252A mutant, we introduced the H116A and E252A mutations into the wild-type PDB (2SHP) using the Mutagenesis Wizard functionality in Pymol Version 2.6. This mutant was simulated using the same CpHMD protocol as for the WT protein.

Statistical analysis

GraphPad Prism was used to prepare graphs and perform statistical analyses. Normality tests were performed on all data sets as well as outlier tests using the ROUT method (Q=1%). Normally distributed data is shown with means and non-normally distributed data is shown with medians. For normally distributed data, significance was determined by ratio paired t-tests or appropriate ANOVA. For non-normally distributed data, significance was determined by Kruskal-Wallis test. In all statistical tests, appropriate multiple comparisons corrections were

913 performed. “N” indicates the number of biological replicates performed and “n” represents the
914 number of technical replicates or individual cell measurements collected.
915
916 **References:**

917 1. Boron, W. F. Regulation of intracellular pH. *Adv. Physiol. Educ.* **28**, 160–179 (2004).
918 2. Spear, J. S. & White, K. A. Single-cell intracellular pH dynamics regulate the cell cycle by
919 timing the G1 exit and G2 transition. *J. Cell Sci.* **136**, jcs260458 (2023).
920 3. Putney, L. K. & Barber, D. L. Na-H Exchange-dependent Increase in Intracellular pH Times
921 G2/M Entry and Transition. *J. Biol. Chem.* **278**, 44645–44649 (2003).
922 4. Frantz, C., Karydis, A., Nalbant, P., Hahn, K. M. & Barber, D. L. Positive feedback between
923 Cdc42 activity and H+ efflux by the Na-H exchanger NHE1 for polarity of migrating cells. *J.*
924 *Cell Biol.* **179**, 403–410 (2007).
925 5. Boussouf, A. & Gaillard, S. Intracellular pH changes during oligodendrocyte differentiation
926 in primary culture. *J. Neurosci. Res.* **59**, 731–739 (2000).
927 6. Czowski, B. J., Romero-Moreno, R., Trull, K. J. & White, K. A. Cancer and pH Dynamics:
928 Transcriptional Regulation, Proteostasis, and the Need for New Molecular Tools. *Cancers*
929 **12**, 2760 (2020).
930 7. Garcia-Moreno, B. Adaptations of proteins to cellular and subcellular pH. *J. Biol.* **8**, 98
931 (2009).
932 8. Harms, M. J. *et al.* A buried lysine that titrates with a normal pKa: role of conformational
933 flexibility at the protein-water interface as a determinant of pKa values. *Protein Sci* **17**, 833–
934 45 (2008).

935 9. Harms, M. J. *et al.* The pK(a) values of acidic and basic residues buried at the same internal
936 location in a protein are governed by different factors. *J Mol Biol* **389**, 34–47 (2009).
937 10. Isom, D. G., Castaneda, C. A., Cannon, B. R. & Garcia-Moreno, B. Large shifts in pKa
938 values of lysine residues buried inside a protein. *Proc Natl Acad Sci U A* **108**, 5260–5
939 (2011).
940 11. Isom, D. G. & Dohlman, H. G. Buried ionizable networks are an ancient hallmark of G
941 protein-coupled receptor activation. *Proc. Natl. Acad. Sci.* **112**, 5702–5707 (2015).
942 12. Isom, D. G. *et al.* Protons as Second Messenger Regulators of G Protein Signaling. *Mol. Cell*
943 **51**, 531–538 (2013).
944 13. Tews, I. *et al.* The Structure of a pH-Sensing Mycobacterial Adenylyl Cyclase Holoenzyme.
945 *Science* **308**, 1020–1023 (2005).
946 14. Olsson, M. H. M., Søndergaard, C. R., Rostkowski, M. & Jensen, J. H. PROPKA3:
947 Consistent Treatment of Internal and Surface Residues in Empirical p K_a Predictions. *J.*
948 *Chem. Theory Comput.* **7**, 525–537 (2011).
949 15. Bertalan, É., Rodrigues, M. J., Schertler, G. F. X. & Bondar, A. Graph-based algorithms to
950 dissect long-distance water-mediated H-bond networks for conformational couplings in
951 GPCRs. *Br. J. Pharmacol.* bph.16387 (2024) doi:10.1111/bph.16387.
952 16. Qu, C. K. The SHP-2 tyrosine phosphatase: Signaling mechanisms and biological functions.
953 *Cell Res.* **10**, 279–288 (2000).
954 17. Mannell, H. & Krotz, F. SHP-2 Regulates Growth Factor Dependent Vascular Signalling and
955 Function. *Mini-Rev. Med. Chem.* **14**, 471–483 (2014).
956 18. Lauriol, J., Jaffré, F. & Kontaridis, M. I. The role of the protein tyrosine phosphatase SHP2
957 in cardiac development and disease. *Semin. Cell Dev. Biol.* **37**, 73–81 (2015).

958 19. Merritt, R., Hayman, M. J. & Agazie, Y. M. Mutation of Thr466 in SHP2 abolishes its
959 phosphatase activity, but provides a new substrate-trapping mutant. *Biochim. Biophys. Acta*
960 *BBA - Mol. Cell Res.* **1763**, 45–56 (2006).
961 20. Schaffhausen, B. SH2 domain structure and function. *Biochim. Biophys. Acta BBA - Rev.*
962 *Cancer* **1242**, 61–75 (1995).
963 21. Hof, P., Pluskey, S., Dhe-Paganon, S., Eck, M. J. & Shoelson, S. E. Crystal Structure of the
964 Tyrosine Phosphatase SHP-2. *Cell* **92**, 441–450 (1998).
965 22. Srivastava, J. *et al.* Structural model and functional significance of pH-dependent talin-actin
966 binding for focal adhesion remodeling. *Proc Natl Acad Sci U A* **105**, 14436–41 (2008).
967 23. Vercoulen, Y. *et al.* A histidine pH sensor regulates activation of the Ras-specific guanine
968 nucleotide exchange factor RasGRP1. *Elife* **6**, e29002 (2017).
969 24. Yariv, B. *et al.* Using evolutionary data to make sense of macromolecules with a "face-
970 lifted" ConSurf. *Protein Sci.* **32**, e4582 (2023).
971 25. Henderson, J. A. *et al.* A Guide to the Continuous Constant pH Molecular Dynamics
972 Methods in Amber and CHARMM [Article v1.0]. *Living J. Comput. Mol. Sci.* **4**, (2022).
973 26. Sun, J. *et al.* Antagonism between binding site affinity and conformational dynamics tunes
974 alternative cis-interactions within Shp2. *Nat. Commun.* **4**, 2037 (2013).
975 27. Cai, T., Nishida, K., Hirano, T. & Khavari, P. A. Gab1 and SHP-2 promote Ras/MAPK
976 regulation of epidermal growth and differentiation. *J. Cell Biol.* **159**, 103–112 (2002).
977 28. Farahani, P. E. *et al.* pYtags enable spatiotemporal measurements of receptor tyrosine kinase
978 signaling in living cells. *eLife* **12**, e82863 (2023).
979 29. Hellmuth, K. *et al.* Specific inhibitors of the protein tyrosine phosphatase Shp2 identified by
980 high-throughput docking. *Proc. Natl. Acad. Sci.* **105**, 7275–7280 (2008).

981 30. Singer, A. U. & Forman-Kay, J. D. pH Titration studies of an SH2 domain-phosphopeptide
982 complex: Unusual histidine and phosphate p K_a values. *Protein Sci.* **6**, 1910–1919 (1997).
983 31. Vogel, H. J. [13] Phosphorus-31 nuclear magnetic resonance of phosphoproteins. in *Methods*
984 *in Enzymology* vol. 177 263–282 (Elsevier, 1989).
985 32. Kurochkina, N. & Guha, U. SH3 domains: modules of protein–protein interactions. *Biophys.*
986 *Rev.* **5**, 29–39 (2013).
987 33. Xu, W., Doshi, A., Lei, M., Eck, M. J. & Harrison, S. C. Crystal Structures of c-Src Reveal
988 Features of Its Autoinhibitory Mechanism. *Mol. Cell* **3**, 629–638 (1999).
989 34. Sondka, Z. *et al.* COSMIC: a curated database of somatic variants and clinical data for
990 cancer. *Nucleic Acids Res.* **52**, D1210–D1217 (2024).
991 35. White, K. A. *et al.* Cancer-associated arginine-to-histidine mutations confer a gain in pH
992 sensing to mutant proteins. *Sci. Signal.* **10**, eaam9931 (2017).
993 36. Kisor, K. pH-Sensors Regulating Transcription, Metabolism, and Cancer Cell Biology.
994 (2023).
995 37. Luna, L. A. *et al.* An acidic residue buried in the dimer interface of isocitrate dehydrogenase
996 1 (IDH1) helps regulate catalysis and pH sensitivity. *Biochem. J.* **477**, 2999–3018 (2020).
997 38. Webb, B. A. *et al.* A Histidine Cluster in the Cytoplasmic Domain of the Na-H Exchanger
998 NHE1 Confers pH-sensitive Phospholipid Binding and Regulates Transporter Activity. *J*
999 *Biol Chem* **291**, 24096–24104 (2016).
1000 39. Chen, A. Y., Lee, J., Damjanovic, A. & Brooks, B. R. Protein p K_a Prediction by Tree-Based
1001 Machine Learning. *J. Chem. Theory Comput.* **18**, 2673–2686 (2022).
1002 40. Ulmschneider, B. *et al.* Increased intracellular pH is necessary for adult epithelial and
1003 embryonic stem cell differentiation. *J Cell Biol* **215**, 345–355 (2016).

1004 41. Liu, Y. *et al.* Intracellular pH dynamics regulates intestinal stem cell lineage specification.
1005 *Nat. Commun.* **14**, 3745 (2023).
1006 42. Amith, S. R., Wilkinson, J. M. & Fliegel, L. Na+/H+ exchanger NHE1 regulation modulates
1007 metastatic potential and epithelial-mesenchymal transition of triple-negative breast cancer
1008 cells. *Oncotarget* **7**, 21091–113 (2016).
1009 43. Suzuki, A., Maeda, T., Baba, Y., Shimamura, K. & Kato, Y. Acidic extracellular pH
1010 promotes epithelial mesenchymal transition in Lewis lung carcinoma model. *Cancer Cell Int.*
1011 **14**, (2014).
1012 44. White, K. A., Grillo-Hill, B. K. & Barber, D. L. Cancer cell behaviors mediated by
1013 dysregulated pH dynamics at a glance. *J. Cell Sci.* **130**, 663–669 (2017).
1014 45. Harguindey, S., Reshkin, S. J., Orive, G., Arranz, J. L. & Anitua, E. Growth and trophic
1015 factors, pH and the Na+/H+ exchanger in Alzheimer's disease, other neurodegenerative
1016 diseases and cancer: new therapeutic possibilities and potential dangers. *Curr Alzheimer Res*
1017 **4**, 53–65 (2007).
1018 46. O'Reilly, A. M., Pluskey, S., Shoelson, S. E. & Neel, B. G. Activated Mutants of SHP-2
1019 Preferentially Induce Elongation of *Xenopus* Animal Caps. *Mol. Cell. Biol.* **20**, 299–311
1020 (2000).
1021 47. Choi, C.-H., Webb, B. A., Chimenti, M. S., Jacobson, M. P. & Barber, D. L. pH sensing by
1022 FAK-His58 regulates focal adhesion remodeling. *J. Cell Biol.* **202**, 849–859 (2013).
1023 48. Case, D. A. *et al.* Amber 2022. Unpublished https://doi.org/10.13140/RG.2.2.31337.77924
1024 (2022).
1025 49. Roe, D. R. & Cheatham, T. E. PTRAJ and CPPTRAJ: Software for Processing and Analysis
1026 of Molecular Dynamics Trajectory Data. *J. Chem. Theory Comput.* **9**, 3084–3095 (2013).

Acknowledgements.
This research was supported in part by the Notre Dame Center for Research Computing; we specifically thank Dr. Dodi Heryadi and Dr. Scott Hampton for technical support.

Funding
This work was supported by:
NSF CAREER AWARD (MCB-2238694) to KAW
NIH New Innovator Award (DP2-CA26041601) to KAW
NIH R01 (R01GM123338) to JWP.

Author contributions.
PKVD contributed to project conceptualization, methodology development, data collection, analysis, figure generation, writing (original draft and review/editing).
LP contributed to methodology development, data collection, analysis, figure generation, and writing (original draft and review/editing.
EAG contributed to data collection, analysis, figure generation, writing (review/editing).
ETN contributed to data collection, analysis, figure generation, writing (review/editing).
JAA contributed to data collection, analysis, writing (review/editing).
LMH contributed to contributed to data collection, analysis, writing (review/editing).
JWP contributed to writing (original draft and review/editing), supervision, and funding acquisition.
KAW contributed to project conceptualization, methodology development, analysis, figure generation, writing (original draft and review/editing), project administration, supervision, and funding acquisition.

Competing interests.

The authors declare no competing interests.

Materials & Correspondence.

For materials requests and correspondence contact Katharine White (kwhite6@nd.edu)